Magnetotelluric responses of three-dimensional conductive and magnetic anisotropic anomalies

Tiaojie Xiao[1,2,3]*, Yun Wang[2,3], Xiangyu Huang[4], Guoli He[5] and Jie Liu[1]

[1]*Science and Technology on Parallel and Distributed Processing Laboratory, National University of Defense Technology, Changsha 410073, China*, [2]*State Key Laboratory of Ore Deposit Geochemistry, Institute of Geochemistry, Chinese Academy of Sciences, Guiyang 550002, China*, [3]*University of Chinese Academy of Sciences, Beijing 100049, China*, [4]*School of Geosciences and Info-Physics, Central South University, Changsha 410083, China, and* [5]*Key Laboratory of Shale Gas and Geoengineering, Institute of Geology and Geophysics, Chinese Academy of Sciences, Beijing 10029, China*

ABSTRACT

A magnetotelluric finite-element modelling algorithm is developed, which is capable of handling three-dimensional conductive and magnetic anisotropic anomalies. Different from earlier three-dimensional magnetotelluric anisotropic modelling methods, the algorithm we presented has taken the magnetic anisotropy into consideration. The variational equations are produced by the Galerkin method and the governing equations are solved using a hexahedral vector edge finite-element method. The accuracy of this algorithm is firstly validated by comparing its solutions with the results of finite-difference method for a three-dimensional conductive arbitrary anisotropic model, and then validated by comparing with analytical solutions for a one-dimensional magnetic model. The responses of four kinds of models under different conditions are studied, and some conclusions are obtained. It shows that for materials with a high magnetic permeability, its influence on magnetotelluric responses cannot be ignored in some circumstances. Especially, if the magnetic susceptibility is exceptionally high, it may really distort the apparent resistivities of lower resistive anomalies. These conclusions are also beneficial for magnetotelluric survey.

Key words: 3D modelling, Conductivity anisotropy, Finite-element method, Magnetotelluric, Magnetic anisotropy.

1 INTRODUCTION

The simulation of geologic structures to magnetotelluric (MT) response has been widely used in several areas of applied geophysics such as exploration of oil and gas and the investigation of deep Earth electrical structures (Mitsuhata, Matsuo and Minegishi 1999; Unsworth *et al.* 2000; Heinson, Direen and Gill 2006; Farquharson and Craven 2009; Hu *et al.* 2013; Spichak *et al.* 2015; Villain *et al.* 2015). Therefore, it is important to study the responses of electromagnetic (EM) fields (Everett 2012; Ren *et al.* 2013; Cai *et al.* 2014; Ren *et al.* 2014; Li, Farquharson and Hu 2016). The behaviour of EM

fields depends on three physical properties of the subsurface (Mukherjee and Everett 2011): electrical conductivity σ, magnetic permeability μ and dielectric permittivity ε. For the frequencies utilized in MT survey, Maxwell's equations are simplified to their magnetoquasistatic limit where displacement currents are neglected, and the magnetic permeability is usually set to be the free-space permeability μ_0. In isotropic media, though most cases have not taken magnetic permeability into consideration, there are still many studies that have taken it into account (Kao and Orr 1982; Zhang and Oldenburg 1997; Zhdanov and Pavlov 2001; Sasaki, Kim and Cho 2010; Mukherjee and Everett 2011; Noh *et al.* 2016).

Conductive anisotropy has become an important research topic in geophysics (Huo *et al.* 2015; Wang *et al.*

2016; Cai *et al.* 2017; Wang and Tan 2017) and numerous researches have shown that the Earth is conductive anisotropic (Marin *et al.* 1998; Klein and Santamarina 2003; Linde and Pedersen 2004; Wannamaker 2005). The phenomenon of anisotropy occurs on various scales due to the preferred orientation within crystals and the inability to resolve ordered inhomogeneity (Weidelt, Oristaglio and Spies 1999; Løseth and Ursin 2007; Martí 2014). In MT survey of the subsurface, the conductive anisotropy will almost certainly affect the EM responses to some extent (Løseth and Ursin 2007). For one-dimensional (1D) and two-dimensional (2D) media, many studies have been carried out (O'Brien and Morrison 1967; Reddy and Rankin 1971; Pek and Verner 1997; Yin 2000; Li 2002; Pek and Santos 2002; Yin 2003, 2006; Li and Pek 2008). For three-dimensional (3D) media, many researches have also been done (Martinelli and Osella 1997; Li 2000). Recently, Xiao *et al.* (2018) presented an edge-based finite-element (FE) algorithm which is capable of simulating MT responses in 3D generalized conductive anisotropic media, and obtained some conclusions; Kong *et al.* (2018) did some qualitative and quantitative analyses for some synthetic conductive anisotropic models based on the staggered-grid finite-difference (FD) method; Liu, Xu and Li (2018) developed an adaptive unstructured edge-based FE method using tetrahedral meshes which is capable of handling of irregular anomalies and topography; Cao *et al.* (2018) also presented a goal-oriented adaptive unstructured FE algorithm that is able to simulate topography and irregular anomalies. However, these studies only focus on the conductive anisotropy while the magnetic anisotropy is not taken into consideration. Besides, there are many studies about magnetic anisotropy (Hrouda 1982; Emerson, Clark and Saul 1985; Rochette, Jackson and Aubourg 1992; Hunt, Moskowitz and Banerjee 1995; Starostenko *et al.* 2009; Kontny *et al.* 2012; Bolle *et al.* 2014; Biedermann and McEnroe 2017). Although conductive anisotropy and magnetic anisotropy both are important, the effects of magnetic anisotropy have only gained little attention in MT modelling so far. It is therefore necessary to study MT responses of 3D conductive and magnetic anisotropic anomalies.

The goal of this paper is to study the MT responses of 3D anomalies which not only are conductive anisotropy but also are magnetic anisotropy. We therefore presented a numerical algorithm for simulating the MT response of conductive and magnetic anisotropic bodies buried within a conductive medium. An FE method using vector edge basis functions is utilized to solve the diffusive governing equations as the inherent disadvantages of the nodal FE method (Ansari
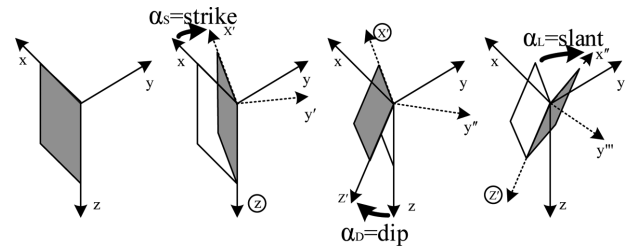

Figure 1 Illustration of basic anisotropic parameters (Pek and Santos 2002): transformation of observation coordinate (xyz) into principal anisotropy coordinate (x'', y''', z') by successively applying three elementary Euler's rotations α_S, α_D and α_L.

and Farquharson 2014). We initially presented the MT forward modelling problem using the Galerkin method with Dirichlet boundary conditions, and validated the algorithm implementation against FD results for a 3D conductive anisotropic model and then against analytical solutions for a 1D magnetic model. We finally simulated the responses of several models, and obtained several conclusions which are beneficial for MT survey.

2 ANISOTROPY

As the conductivity tensor is symmetrical, it can therefore be expressed by three principal conductivities and a rotation matrix which can be decomposed into three elementary Euler spatial rotations (Pek and Santos 2002). Similarly to the definition of the anisotropic conductivity tensor, the anisotropic magnetic susceptibility tensor can also be defined by three principal magnetic susceptibilities and three Euler angles. As showed in Fig. 1, three Euler angles (i.e. α_S, α_D and α_L) are identified with the anisotropy strike, dip and slant, respectively.

$$
\tilde{\lambda} = \begin{bmatrix} \lambda_{xx} & \lambda_{xy} & \lambda_{xz} \\ \lambda_{yx} & \lambda_{yy} & \lambda_{yz} \\ \lambda_{zx} & \lambda_{zy} & \lambda_{zz} \end{bmatrix} = \mathbf{R}_z(-\alpha_S)\mathbf{R}_x(-\alpha_D)\mathbf{R}_z(-\alpha_L)
$$

$$
\begin{bmatrix} \lambda_x & 0 & 0 \\ 0 & \lambda_y & 0 \\ 0 & 0 & \lambda_z \end{bmatrix} \mathbf{R}_z(\alpha_L)\mathbf{R}_x(\alpha_D)\mathbf{R}_z(\alpha_S). \tag{1}
$$

In this expression, $\tilde{\lambda}$ denotes the conductivity tensor or the magnetic susceptibility tensor and $\mathbf{R}$ is the elementary rotation matrix.

$$
\mathbf{R}_z(\alpha) = \begin{bmatrix} \cos\alpha & \sin\alpha & 0 \\ -\sin\alpha & \cos\alpha & 0 \\ 0 & 0 & 0 \end{bmatrix},
$$

$$\mathbf{R}_x(\alpha) = \begin{bmatrix} 1 & 0 & 0 \\ 0 & \cos\alpha & \sin\alpha \\ 0 & -\sin\alpha & \cos\alpha \end{bmatrix}. \tag{2}$$

Therefore, the conductivity tensor and the magnetic susceptibility tensor can be revised as follows:

$$\tilde{\sigma} = \begin{bmatrix} \sigma_{xx} & \sigma_{xy} & \sigma_{xz} \\ \sigma_{yx} & \sigma_{yy} & \sigma_{yz} \\ \sigma_{zx} & \sigma_{zy} & \sigma_{zz} \end{bmatrix}, \tag{3}$$

and

$$\tilde{\chi} = \begin{bmatrix} \chi_{xx} & \chi_{xy} & \chi_{xz} \\ \chi_{yx} & \chi_{yy} & \chi_{yz} \\ \chi_{zx} & \chi_{zy} & \chi_{zz} \end{bmatrix}. \tag{4}$$

The magnetic tensor then can be expressed as follows:

$$\tilde{\mu} = \mu_0 \tilde{\mu}_r = \mu_0 \begin{bmatrix} \mu_{xx} & \mu_{xy} & \mu_{xz} \\ \mu_{yx} & \mu_{yy} & \mu_{yz} \\ \mu_{zx} & \mu_{zy} & \mu_{zz} \end{bmatrix}$$

$$= \mu_0 \begin{bmatrix} 1+\chi_{xx} & \chi_{xy} & \chi_{xz} \\ \chi_{yx} & 1+\chi_{yy} & \chi_{yz} \\ \chi_{zx} & \chi_{zy} & 1+\chi_{zz} \end{bmatrix}. \tag{5}$$

3 FINITE ELEMENT METHOD

3.1 Variational equation

We assume a harmonic time dependence of $e^{-i\omega t}$ and neglect the displacement current for frequencies utilized in magnetotelluric survey. Thus, Maxwell's equations in the frequency domain are as follows (Løseth and Ursin 2007):

$$\nabla \times \mathbf{E} = i\omega\tilde{\mu}\mathbf{H}, \tag{6}$$

$$\nabla \times \mathbf{H} = \tilde{\sigma}\mathbf{E}, \tag{7}$$

$$\nabla \cdot \tilde{\mu}\mathbf{H} = 0, \tag{8}$$

and

$$\nabla \cdot \varepsilon\mathbf{E} = \rho_Q. \tag{9}$$

In these expressions, $\mathbf{E}$ denotes the electric field, $\mathbf{H}$ denotes the magnetic field, i is $\sqrt{-1}$, ω is the angular frequency, ε is the dielectric constant, ρ_Q is the accumulated charge, $\tilde{\mu}$ is the magnetic permeability tensor and $\tilde{\sigma}$ is the conductivity tensor.
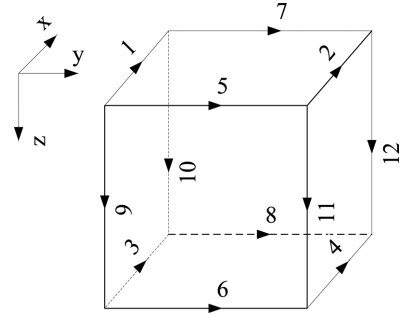

Figure 2 A hexahedral cell: the electric fields are located at the 12 edges.

Combining equation (6) with equation (7), equation (10) can be obtained as follows:

$$\nabla \times (\tilde{v}\nabla \times \mathbf{E}) - i\omega\tilde{\sigma}\mathbf{E} = 0. \tag{10}$$

In equation (10), $\tilde{v}$ is the magnetic reluctivity tensor and $\tilde{v} = \tilde{\mu}^{-1}$ (Bardi and Biro 1991).

The Galerkin weighted residuals method (Xu 1994) was then adopted to generate the variational equation. Multiplying both sides of equation (10) by $\delta\mathbf{E}$ and integrating across all cells, besides considering the vector identity and the divergence theorem together, equation (11) then can be obtained as follows:

$$\int_v \nabla \times \delta\mathbf{E} \cdot (\tilde{v}\nabla \times \mathbf{E})\,dv - \int_v i\omega\tilde{\sigma}\mathbf{E} \cdot \delta\mathbf{E}dv + \int_\Gamma (\tilde{v}\nabla \times \mathbf{E})$$

$$\times \delta\mathbf{E} \cdot d\mathbf{\Gamma} = 0, \tag{11}$$

where $\delta\mathbf{E}$ is the variation of $\mathbf{E}$, $\delta\mathbf{E} = \delta\mathbf{E}_x + \delta\mathbf{E}_y + \delta\mathbf{E}_z$ (Xu 1994). At outer boundaries, the second integration of equation (11) equals 0 as the Dirichlet boundary condition was adopted; at inner boundaries, it is also 0 because of counteraction. Equation (11) therefore can be rewritten as follows:

$$\int_v \nabla \times \delta\mathbf{E} \cdot (\tilde{v}\nabla \times \mathbf{E})\,dv - \int_v i\omega\tilde{\sigma}\mathbf{E} \cdot \delta\mathbf{E}dv = 0. \tag{12}$$

3.2 The edge-based finite-element method

For the edge-based finite-element (FE) method, the electric fields are located at 12 edges of each cell as showed in Fig. 2.

The electric fields then can be expressed as follows:

$$\mathbf{E}_x^e = \sum_{i=1}^4 N_{xi}^e \mathbf{E}_{xi}^e, \quad \mathbf{E}_y^e = \sum_{j=1}^4 N_{yi}^e \mathbf{E}_{yi}^e, \quad \mathbf{E}_z^e = \sum_{k=1}^4 N_{zi}^e \mathbf{E}_{zi}^e. \tag{13}$$

In this expression, N denotes the Whitney vector basis (see Jin 2002, for details), and

$$\mathbf{E}^T = \begin{bmatrix} \mathbf{E}_x^e & \mathbf{E}_y^e & \mathbf{E}_z^e \end{bmatrix}, \, \delta\mathbf{E}^T = \begin{bmatrix} \delta\mathbf{E}_x^e & \delta\mathbf{E}_y^e & \delta\mathbf{E}_z^e \end{bmatrix}. \tag{14}$$

Because N has a zero divergence – that is $\nabla \cdot \mathbf{N}_i^e = 0$, therefore edge-based FE method is divergence-free in each element (Jin 2002). Calculating each integral in equation (12) for every element, the following matrix expression can be obtained:

$$\sum_{n=1}^{n_e} \int_e \nabla \times \delta\mathbf{E} \cdot (\tilde{v}\nabla \times \mathbf{E}) \, \mathrm{d}v - \sum_{n=1}^{n_e} \int_e i\omega\tilde{\sigma}\mathbf{E} \cdot \delta\mathbf{E}\mathrm{d}v = 0. \tag{15}$$

According to equation (15), it is obvious that the magnetic permeability tensor only affect the first integration of equation (15).

For a given element, the first integration of equation (15) changes into

$$\int_e \nabla \times \delta\mathbf{E} \cdot (\tilde{v}\nabla \times \mathbf{E}) \, \mathrm{d}v$$

$$= \int_e \left\{ \delta\mathbf{E}^T \begin{bmatrix} 0 & \dfrac{\partial N_x^e}{\partial z} & -\dfrac{\partial N_x^e}{\partial y} \\[2ex] -\dfrac{\partial N_y^e}{\partial z} & 0 & \dfrac{\partial N_y^e}{\partial x} \\[2ex] \dfrac{\partial N_z^e}{\partial y} & -\dfrac{\partial N_z^e}{\partial x} & 0 \end{bmatrix} \begin{bmatrix} v_{xx} & v_{xy} & v_{xz} \\[1ex] v_{yx} & v_{yy} & v_{yz} \\[1ex] v_{zx} & v_{zy} & v_{zz} \end{bmatrix} \right.$$

$$\left. \times \begin{bmatrix} 0 & -\left(\dfrac{\partial N_y^e}{\partial z}\right)^T & \left(\dfrac{\partial N_z^e}{\partial y}\right)^T \\[2ex] \left(\dfrac{\partial N_x^e}{\partial z}\right)^T & 0 & -\left(\dfrac{\partial N_z^e}{\partial x}\right)^T \\[2ex] -\left(\dfrac{\partial N_x^e}{\partial y}\right)^T & \left(\dfrac{\partial N_y^e}{\partial x}\right)^T & 0 \end{bmatrix} \mathbf{E} \right\} \mathrm{d}v$$

$$= (\delta\mathbf{E}_e)^T \mathbf{K}_{1e}\mathbf{E}_e. \tag{16}$$

The specific values of $\mathbf{K}_{1e}$ are given in Appendix A. The second integration of equation (15) turns into

$$-\int_e i\omega\tilde{\sigma}\mathbf{E} \cdot \delta\mathbf{E}\mathrm{d}v \tag{17}$$

$$= -i\omega\mu \int_e \left\{ \delta\mathbf{E}^T \begin{bmatrix} N_x^e & 0 & 0 \\ 0 & N_y^e & 0 \\ 0 & 0 & N_z^e \end{bmatrix} \begin{bmatrix} \sigma_{xx} & \sigma_{xy} & \sigma_{xz} \\ \sigma_{yx} & \sigma_{yy} & \sigma_{yz} \\ \sigma_{zx} & \sigma_{zy} & \sigma_{zz} \end{bmatrix} \right.$$

$$\left. \times \begin{bmatrix} (N_x^e)^T & 0 & 0 \\ 0 & (N_y^e)^T & 0 \\ 0 & 0 & (N_z^e)^T \end{bmatrix} \mathbf{E} \right\} \mathrm{d}v$$

$$= (\delta\mathbf{E}_e)^T \mathbf{K}_{2e}\mathbf{E}_e. \tag{18}$$

The specific values of $\mathbf{K}_{2e}$ are given in Appendix A. We added equation (16) to equation (18) and expanded it to all elements. Then equation (19) was obtained as follows:

$$\delta\mathbf{E}^T \left[\sum_{e=1}^{n_e} (\bar{\mathbf{K}}_{1e} + \bar{\mathbf{K}}_{2e}) \right] \mathbf{E} = 0. \tag{19}$$

Adding the Dirichlet boundary conditions into equation (19) and considering $\delta\mathbf{E}^T$ can be any values, finally equation (20) can be obtained:

$$\mathbf{KE} = \mathbf{P}, \tag{20}$$

where $\mathbf{K} = \sum_{e=1}^{n_e} (\bar{\mathbf{K}}_{1e} + \bar{\mathbf{K}}_{2e})$, and $\mathbf{P}$ is composed of the last term of equation (19) and the Dirichlet boundary conditions.

Two orthogonal sources A and B are located on the top surface of the research area: $\mathbf{E}_A = (\mathbf{E}_A^x, \mathbf{E}_A^y, \mathbf{E}_{SA}^z) = (1, 0, 0)$, $\mathbf{E}_B = (\mathbf{E}_B^x, \mathbf{E}_B^y, \mathbf{E}_B^z) = (0, 1, 0)$. Because there is no appropriate modelling magnetotelluric code for one-dimensional (1D) or two-dimensional conductive and magnetic anisotropic media, the Dirichlet boundary conditions here are obtained by 1D conductive anisotropic analytical computation (Pek and Santos 2002), which is unable to handle magnetic media. After solving equation (20), the unknown electric fields can be obtained. Furthermore, the magnetic fields, the impedance tensor, the apparent resistivities and phases also can be obtained.

4 ACCURACY VALIDATION

For a new algorithm, it should be checked against known equivalent solutions. In order to validate the correctness and accuracy of this algorithm, we divide the validation exercises into two steps: a check against a non-magnetic case and a comparison for a magnetic case. Because the purpose in this section is to validate the method's correctness and accuracy, therefore the magnetotelluric responses here are not analysed in detail.

4.1 Non-magnetic case

This new algorithm's accuracy is firstly validated by comparing its results with the solutions of Kong's *et al.* (2018) FD code for a three-dimensional (3D) arbitrary conductive anisotropic. As shown in Fig. 3, a 3D anomaly is embedded in an isotropic half-space, the dimensions of the anomaly are 1100 m × 1100 m × 1000 m and its top depth is 250 m; the half-space's conductivity is 0.01 S/m and its magnetic susceptibility is 0. In order to test this new algorithm's capability, the anomaly's three Euler's angles all are non-zero and the conductivity contrast is up to 25. Its three principal conductivities
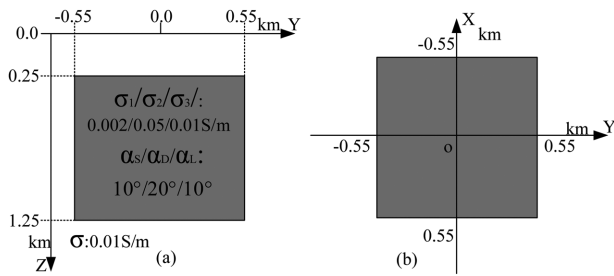
Figure 3 The test model: (a) section view and (b) plan view. In a half-space of 0.01 S/m, there is a 3D anomaly. Its dimensions are 1100 m × 1100 m × 1000 m and its top depth is 250 m. Its three principal conductivities are 0.002 S/m, 0.05 S/m and 0.01 S/m, respectively, and its three Euler angles are 10°, 20° and 10°, respectively.

are 0.002, 0.05 and 0.01 S/m, respectively; its three conductive anisotropic angles are 10°, 20°, and 10°, respectively; and its magnetic susceptibility is 0. Two frequencies (10 Hz and 0.1 Hz) are computed.

Along $y = 0$ m on the earth surface, the total electric fields generated by Source A are shown in Fig. 4 the upper row corresponds to the comparison of finite-element (FE) and finite-difference's (FD) total electric fields' amplitude, and the lower row corresponds to the relative errors; the left column and the second column correspond to 10 and 0.1 Hz,

Figure 5 Along $y = 0$ m on the earth surface, the comparison between FE's and FD's secondary electric fields' amplitude is shown: the upper row corresponds 10 Hz, and the lower row corresponds to 0.1 Hz.

respectively. The results reveal a very close level of agreement as the relative errors are both less than 1.5% for two frequencies. Besides, the secondary electric fields are shown in Fig. 5. The upper plot corresponds to 10 Hz, and the lower

Figure 4 Along $y = 0$ m on the earth surface, the comparison between FE's and FD's total electric fields' amplitude is shown: the left column and the right column correspond to 10 Hz and 0.1 Hz, respectively; the upper row are comparisons of FE and FD, and the lower row are the relative errors.
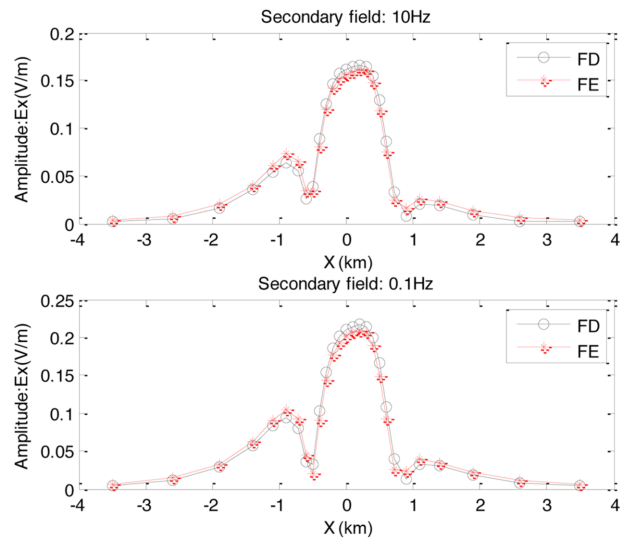
corresponds to 0.1 Hz. It shows that the secondary electric fields of FE and FD agree well. However, the relative errors are not shown here as the secondary field's amplitude has very small values.

The system of equations is large and sparse, and it was solved using a bi-conjugate gradient stabilized solver with a symmetric successive over-relaxation pre-conditioner. The number of elements is 63,878. The codes ran on a 64-bit Windows 7 computer with Intel i7-4790 3.60 GHz processor, and the calculation of this model took 394 seconds at 10 Hz.

4.2 Magnetic case

This new algorithm is again validated by comparing its results with one-dimensional (1D) analytical solutions (Yadav and Lal 1997). As shown in Fig. 6, a three-layered magnetic earth model has been computed. The apparent resistivities and phases are shown in Figs 7 and 8, respectively.

Because the Dirichlet boundaries are generated by 1D conductive anisotropy code (Pek and Santos 2002), which is unable to deal with magnetic media, a three-dimensional (3D) magnetic anomaly is used as an approximation of the magnetic layer. The 3D results at the origin are compared with the 1D analytical solutions. Covering a broad band frequency (0.001–1000 Hz), the apparent resistivities and the phases are shown in Figs 7 and 8, respectively. In order to show the magnetic susceptibility's influence, the results are also shown when the second layer's magnetic susceptibility is 0.

The results including the apparent resistivities and phases show that the numerical results agree well with the analytical solutions as the relative errors of apparent resistivities are all less than 1% and the relative errors of phases are all less than 2%. The results also show that the magnetic susceptibility's influence cannot be ignored for this model, and the positive
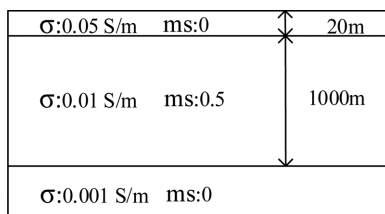

Figure 6 Three-layered magnetic model: the second layer is a magnetized layer with a top depth of 20 m, its magnetic susceptibility is 0.5, conductivity is 0.01 S/m and its thickness is 1000 m; the first layer's conductivity is 0.05 S/m; and the third layer's conductivity is 0.001 S/m (Yadav and Lal 1997).
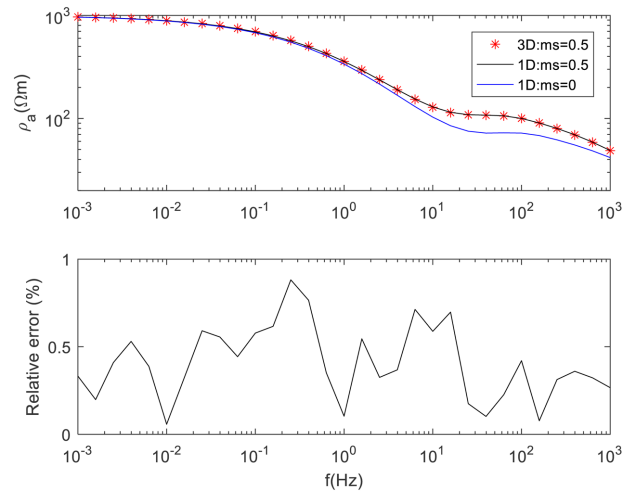

Figure 7 The comparison between 3D and 1D (Yadav and Lal 1997) apparent resistivities is shown. The upper row corresponds to the comparison of 3D and 1D apparent resistivities; the asterisk and the black curve represent the 3D and 1D results when the second layer's magnetic susceptibility is 0.5, respectively, whereas the blue curve represents the 1D solutions when the second layer's magnetic susceptibility is zero. The lower row corresponds to the relative errors between 3D and 1D results when the second layer's magnetic susceptibility is 0.5.
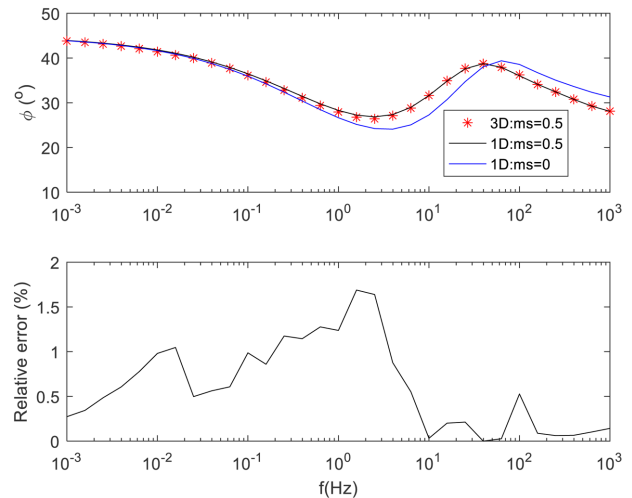

Figure 8 The comparison between 3D and 1D (Yadav and Lal 1997) phases is shown. The upper row corresponds to the comparison of 3D and 1D phases; the asterisk and the black curve represent the 3D and 1D results when the second layer's magnetic susceptibility is 0.5, respectively, whereas the blue curve represents the 1D solutions when the second layer's magnetic susceptibility is zero. The lower row corresponds to the relative errors between 3D and 1D results when the second layer's magnetic susceptibility is 0.5.
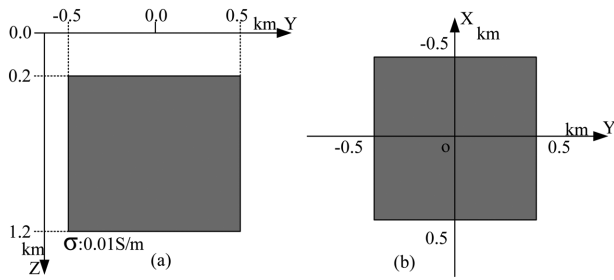
Figure 9 The model: (a) section view (left); (b) plan view (right). A 3D anomaly is embedded in a half-space. Its dimensions are 1000 m × 1000 m × 1000 m and its top depth is 250 m. The background conductivity is 0.01 S/m.

magnetic susceptibility leads to higher apparent resistivities. This phenomenon will be explained later in Section 5.1.

5   NUMERICAL EXPERIMENTS

In order to study the influences of magnetic anisotropic parameters, four models are designed and their responses are studied carefully. As shown in Fig. 9, a three-dimensional (3D) anomaly is embedded in a half-space. The half-space's conductivity is 0.01 S/m and its magnetic susceptibility is 0.

The anomaly's dimensions are 1000 m × 1000 m × 1000 m and its top depth is 200 m. Four models (Model 1 to Model 4) are obtained by changing the 3D anomaly's anisotropic parameters. The computed frequency is 10 Hz in this section. All the magnetic susceptibilities in this section are common susceptibilities (less than 0.5).

5.1   Model 1: magnetic isotropy

The three-dimensional (3D) anomaly of Model 1 is set to be a magnetic isotropic cube, its conductivity is 0.01 S/m and its magnetic susceptibility is set to be -0.3, -0.15, 0, 0.15 and 0.3, respectively. Six frequencies (1000, 100, 10, 1, 0.1 and 0.01 Hz) from high to low are computed, the apparent resistivities of 10 Hz are shown in Fig. 10, and the other results including apparent resistivities and phases are shown in Appendix B (Figs B1–B11). In Fig. 10, the first to fourth rows correspond to xx-, xy-, yx- and yy-mode apparent resistivities, respectively, whereas the first to fifth columns correspond to magnetic susceptibilities of -0.3, -0.15, 0, 0.15 and 0.3, respectively. The black square in this figure represents the 3D anomaly. It shows that the xy- and yx-mode apparent resistivities manifested as lower apparent resistivities
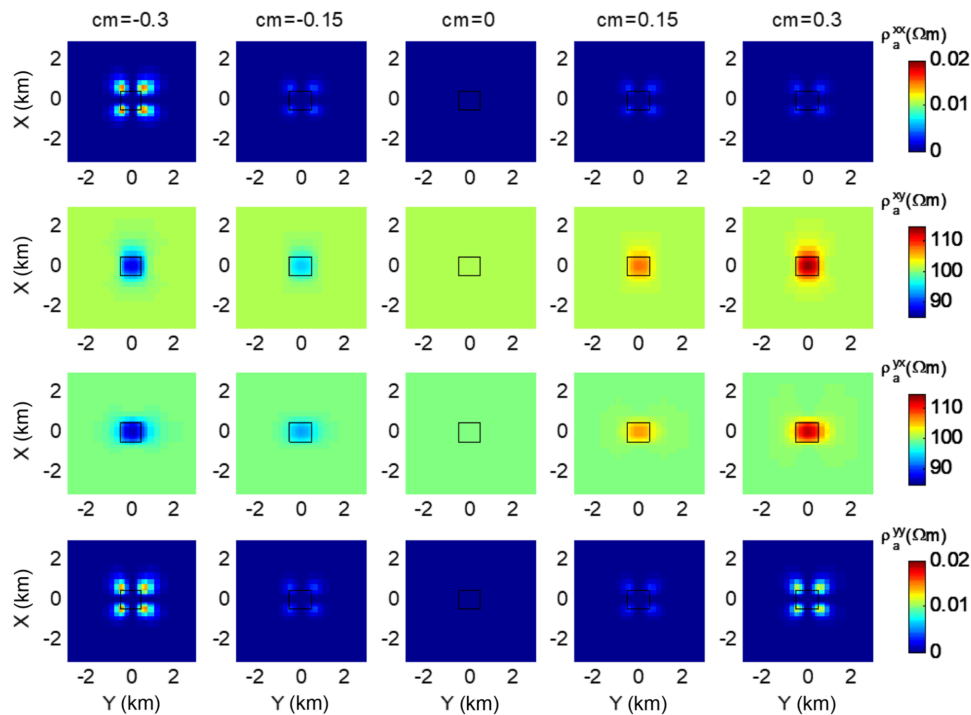

Figure 10 Apparent resistivities of Model 1 with different magnetic susceptibilities at 10 Hz: the first to fourth rows correspond to the apparent resistivities of xx-, xy-, yx- and yy-mode, respectively; the first to fifth columns correspond to magnetic susceptibilities of -0.3, -0.15, 0, 0.15 and 0.3, respectively. The black square represents the 3D anomaly.
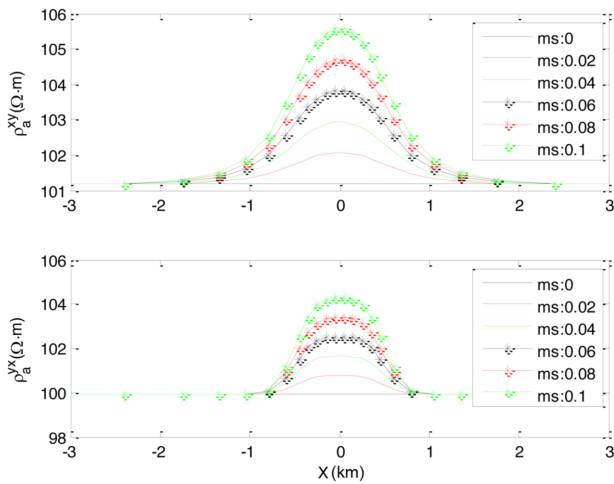
Figure 11 Along $y = 0$ m on the earth surface, apparent resistivities of Model 1 at 10 Hz is shown: the 3D anomaly has different magnetic susceptibilities (0, 0.02, 0.04, 0.06, 0.08 and 0.1), the upper corresponds to the *xy*-mode apparent resistivities and the lower row corresponds to the *yx*-mode apparent resistivities.

to higher apparent resistivities from left to right. Especially, when the magnetic susceptibility is 0, the *xy*- and *yx*-mode apparent resistivities are 100 Ωm, the reason is that Model 1 is a half-space of 0.01 S/m when the magnetic susceptibility is 0. The data show that a negative magnetic susceptibility leads to lower apparent resistivities, and a positive magnetic susceptibility leads to higher apparent resistivities.

Why does this phenomenon occur? A simple isotropic half-space is taken as an example to explain it. In Appendix C, the apparent resistivities in axial conductive and magnetic anisotropic media have been derived. For an isotropic half-space, the magnetic susceptibility is a constant. According to (C14) in Appendix C, the apparent resistivity can be rewritten as $\rho_a = (1 + \chi)\rho$. Therefore, it is safe to conclude that a negative magnetic susceptibility leads to a lower apparent resistivity and a positive magnetic susceptibility leads to a higher apparent resistivity.

To study the threshold of the magnetic susceptibility's influence on the magnetotelluric responses, Model 1 with different susceptibilities of 0, 0.02, 0.04, 0.06, 0.08 and 0.1 at 10 Hz is studied. Along $y = 0$ m on the earth surface, the *xy*- and *yx*-mode apparent resistivities are shown in Fig. 11. The data show that the *xy*-mode apparent resistivities have larger values compared with the *yx*-mode apparent resistivities; when the susceptibility is 0.08, the maximum of the *xy*-mode apparent resistivities is about 105 Ωm and the maximum of the *yx*-mode apparent resistivities is about 104 Ωm.

5.2 Model 2: conductive isotropy and magnetic isotropy

As to Model 2.1, the anomaly is set to be a conductive and magnetic isotropic cube. The conductivity of the anomaly is 1/80 S/m and its magnetic susceptibility is set to 0, 0.1, 0.3 and 0.4, respectively. As shown in Fig. 12, the first to fourth rows correspond to *xx*-, *xy*-, *yx*- and *yy*-mode apparent resistivities, respectively, whereas the first to fifth columns correspond to magnetic susceptibilities of 0, 0.1, 0.2, 0.3 and 0.4, respectively. The data presented in Fig. 12 show the apparent resistivities with different magnetic susceptibilities. Four modes' apparent resistivities all indicate well the location and shape of the anomaly. As the magnetic susceptibility increasing, the *xy*- and *yx*-mode apparent resistivities change from lower to higher. Especially, when the magnetic susceptibility is larger than 0.3, the *xy*- and *yx*-mode apparent resistivities manifested as higher apparent resistivities. It also can be explained by (C14): (1) when the magnetic susceptibility is 0.3, the $(1 + \chi)\rho$ is 104 Ωm; (2) when the magnetic susceptibility is 0.4, the is 112 Ωm. Both are larger than the background resistivity (100 Ωm). Although the $(1 + \chi)\rho$ is smaller than the background resistivity when the susceptibility is smaller than 0.2, it agrees with the conclusions obtained in Section 5.1.

Although the three-dimensional (3D) anomaly's resistivity in Model 2 is lower, due to the influence of the magnetic susceptibility the apparent resistivities may manifest as higher apparent resistivities. For Model 2.1, it can therefore be concluded that a high magnetic susceptibility has a significant influence on the MT responses, even can invert the behaviour of the apparent resistivities.

For Model 2.2, the conductivity of the 3D anomaly is set to be 1 S/m, and three frequencies (100, 50 and 10 Hz) are computed. The apparent resistivities are shown in Appendix B (Figs B12–B14). Because it is not convenient to see the apparent resistivities' differences between different susceptibilities, therefore the apparent resistivities at the centre coordinates (0, 0, 0) are listed in Table 1. For Model 2.2, the susceptibilities change the apparent resistivities' values but not invert its behaviour. For the biggest susceptibility 0.4 utilized in Model 2.2, the $(1 + \chi)\rho$ is 1.4 Ωm, which is far less than the background resistivity. Therefore, the results agree with the conclusions obtained in Section 5.1.

5.3 Model 3: magnetic anisotropy

As to model 3, the anomaly is set to be a magnetic anisotropic cube. Its three principal magnetic susceptibilities are –0.1, 0.1 and 0, respectively. The conditions that the anomaly has different magnetic anisotropic angles are studied.
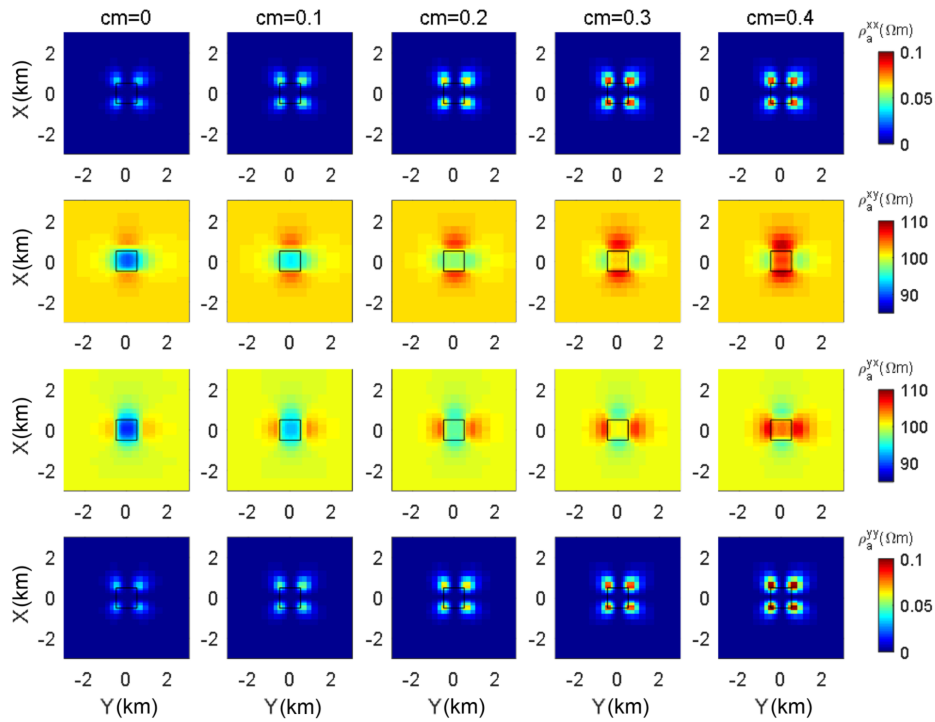
Figure 12 Apparent resistivities of Model 2 with different magnetic susceptibilities at 10 Hz: the first to fourth rows correspond to *xx*-, *xy*-, *yx*- and *yy*-mode apparent resistivities, respectively, whereas the first to fourth columns correspond to magnetic susceptibility of 0, 0.1, 0.2, 0.3 and 0.4, respectively.

5.3.1 α_S changes when α_D and α_L both equal zero

The apparent resistivities with a different angle α_S are shown in Fig. 13. The first to fourth rows correspond to *xx*-, *xy*-, *yx*- and *yy*-mode apparent resistivities, respectively, whereas the first to fourth columns correspond to angles α_S of 0°, 30°, 60° and 90°, respectively. Four modes' apparent resistivities all indicate well the location and shape of the anomaly. There are solid red lines and solid green lines in this figure, the angles between the red lines and the positive *y*-direction are 0°, 30°, 60°, and 90° from left to right, respectively; whereas the angles between the green lines and the positive *x*-direction are

Table 1 The apparent resistivities of Model 2.2 at the centre coordinates (0, 0, 0): three frequencies are computed (100, 50 and 10 Hz), and the apparent resistivities of the anomaly with different susceptibilities (0 and 0.4) are compared

Frequency (Hz)	ρ_{xy} (Ωm)		ρ_{yx} (Ωm)	
	χ:0	χ:0.4	χ:0	χ:0.4
100	37.25	38.03	34.27	35.09
50	22.18	23.21	20.39	21.41
10	8.01	8.91	7.38	8.26

0°, 30°, 60° and 90°, respectively. As showed in this figure, the red lines agree with the directions of the lower apparent resistivities, whereas the green lines agree with the directions of the higher apparent resistivities from left to right, respectively. Actually, the red lines represent the principal magnetic susceptibility of 0.1, whereas the green lines represent the principal magnetic susceptibility of –0.1. In addition, the *xy*-mode apparent resistivities change from higher resistivity to lower resistivity, whereas the *yx*-mode apparent resistivities change from lower resistivity to higher resistivity from left to right. Considering the conclusion obtained in Section 5.1, a negative magnetic susceptibility leads to lower apparent resistivities, whereas a positive magnetic susceptibility leads to higher apparent resistivities. Therefore, the reason is that the magnetic susceptibility is negative in the *x*-direction and positive in the *y*-direction when angle α_S is 0°, and is positive in the *x*-direction and negative in the *y*-direction when angle α_S is 90°. It will be explained in Section 5.3.2.

5.3.2 α_D changes when α_S and α_L both equal zero

The apparent resistivities with different angles α_D are presented in Fig. 14. The first to fourth rows correspond to
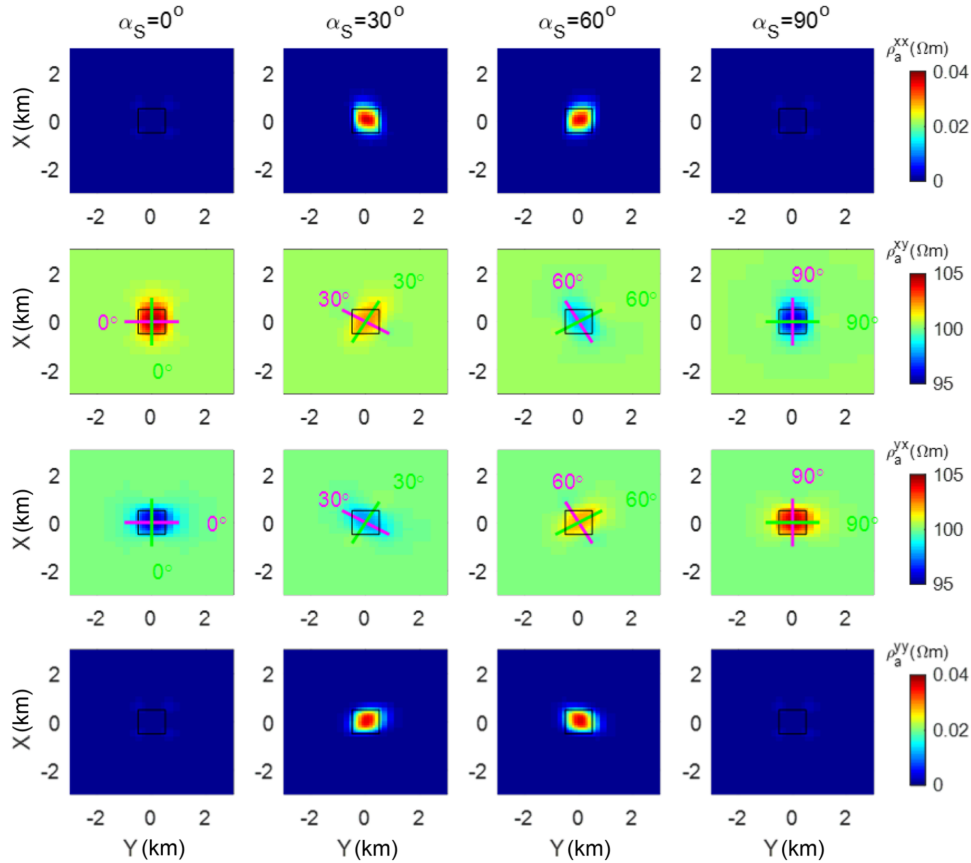
Figure 13 Apparent resistivities of Model 3 with different magnetic anisotropic angles α_S at 10 Hz: the first to fourth rows correspond to *xx*-, *xy*-, *yx*- and *yy*-mode apparent resistivities, respectively, whereas the first to fourth columns correspond to angles α_S of 0°, 30°, 60° and 90°, respectively. The black square represents the anomaly. The angles between the solid red lines and the negative *y*-direction are 0°, 30°, 60° and 90° from left to right, respectively; whereas the angles between the solid green lines and the positive *x*-direction are 0°, 30°, 60° and 90°, respectively.

xx-, *xy*-, *yx*- and *yy*-mode apparent resistivities, respectively, whereas the first to fourth columns correspond to angles α_D of 0°, 30°, 60° and 90°, respectively. The location and shape of the anomaly are well indicated by the apparent resistivities. The *xy*-mode apparent resistivities change significantly, whereas the *yx*-mode apparent resistivities remain almost the same when the angle α_D changes, the reason is that a principal magnetic susceptibility is in the *y*-direction and remain unchanged; when α_D is 90°, the *xy*- and *yy*-mode apparent resistivities show no anomaly, the reason is that the principal magnetic susceptibility of 0 is in the *y*-direction.

Although it is very complex for three-dimensional anisotropic models, a simple axial magnetic anisotropic halfspace can be used as an example to explain these phenomena: according to (C14) and (C15) in Appendix C, the apparent resistivities can be rewritten as $\rho_a^{xy} = (1 + \chi_{yy})\rho$ and

$\rho_a^{yx} = (1 + \chi_{xx})\rho$. Therefore, for magnetic anisotropic models, it can be concluded that: (1) if a principal magnetic susceptibility is in the *x*-direction, then the *yx*-mode apparent resistivities are mainly influenced by this principal magnetic susceptibility; (2) if a principal magnetic susceptibility is in the *y*-direction, then the *xy*-mode apparent resistivities are mainly influenced by this principal magnetic susceptibility.

5.4 Model 4: conductive and magnetic axial anisotropy

For Model 4, the anomaly of Model 4.1 is set to be axial conductive anisotropy and its three principal conductivities are 0.01, 1/80 and 0.0025 S/m, respectively; the anomaly of Model 4.2 is also set to be axial conductive anisotropy and its three principal conductivities are 0.005, 0.02 and 0.0025 S/m, respectively; the anomaly of Model 4.3 is set to be axial
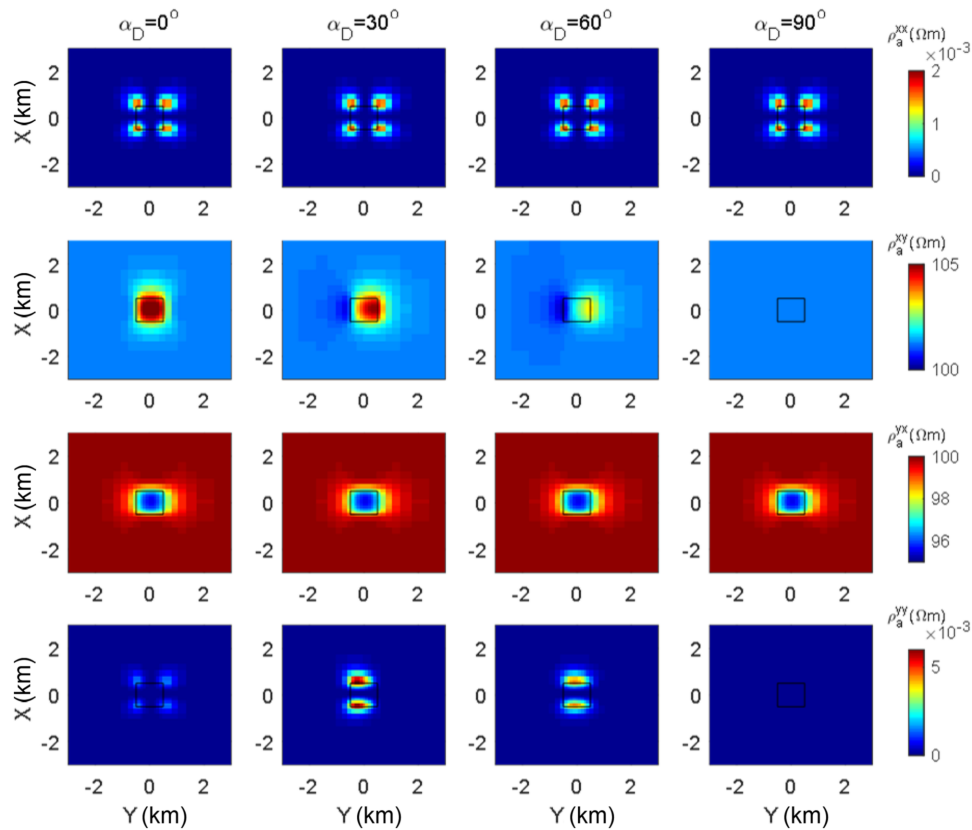
Figure 14 Apparent resistivities of Model 3 with different magnetic anisotropic angles α_D at 10 Hz: the first to fourth rows correspond to *xx*-, *xy*-, *yx*- and *yy*-mode apparent resistivities, respectively, whereas the first to fourth columns correspond to angles α_D of 0°, 30°, 60° and 90°, respectively. The black square represents the anomaly.

magnetic anisotropy, its three principal magnetic susceptibilities are 0.4, –0.1 and 0, respectively; the anomaly of Model 4.4 is set to be axial conductive and magnetic anisotropy, its conductivities and susceptibilities are the same as those of Model 4.1 and Model 4.3, respectively; the anomaly of Model 4.5 is also set to be axial conductive and magnetic anisotropy, and its conductivities and susceptibilities are the same as those of Model 4.2 and Model 4.3, respectively.

As shown in Fig. 15, the first to fourth rows correspond to *xx*-, *xy*-, *yx*- and *yy*-mode apparent resistivities, respectively, whereas the first to fifth columns correspond to Model 4.1, Model 4.2, Model 4.3, Model 4.4 and Model 4.5, respectively. (1) Model 4.1 is axial conductive anisotropy, and the principal resistivity in the *x*-direction is 100 Ωm, which is the same as the background resistivity, and the principal resistivity in the *y*-direction is 80 Ωm, which is smaller than the background resistivity. Therefore, the *xy*-mode apparent resistivities show no anomaly, whereas the *yx*-mode apparent resistivity manifested as lower apparent resistivities. (2)

Model 4.2 is also axial conductive anisotropy. The principal resistivity in the *x*-direction is 200 Ωm, which is larger than the background resistivity, and the principal resistivity in the *y*-direction is 50 Ωm, which is smaller than the background resistivity. Therefore, the *xy*-mode apparent resistivities manifested as higher apparent resistivities, whereas the *yx*-mode apparent resistivities manifested as lower apparent resistivities. (3) Model 4.3 is axial magnetic anisotropy, and the principal magnetic susceptibility in the *y*-direction is –0.1, which is smaller than the background susceptibility, and the principal magnetic susceptibility in the *x*-direction is 0.4, which is larger than the background susceptibility. Therefore the *xy*-mode apparent resistivities manifested as lower apparent resistivities, whereas the *yx*-mode apparent resistivities manifested as higher apparent resistivities. (4) Model 4.4 is axial conductive and magnetic anisotropy, its axial conductivities are the same as Model 4.1 and its axial magnetic susceptibilities are the same as Model 4.3. Due to the influence of the magnetic susceptibilities, the *xy*-mode apparent resistivities
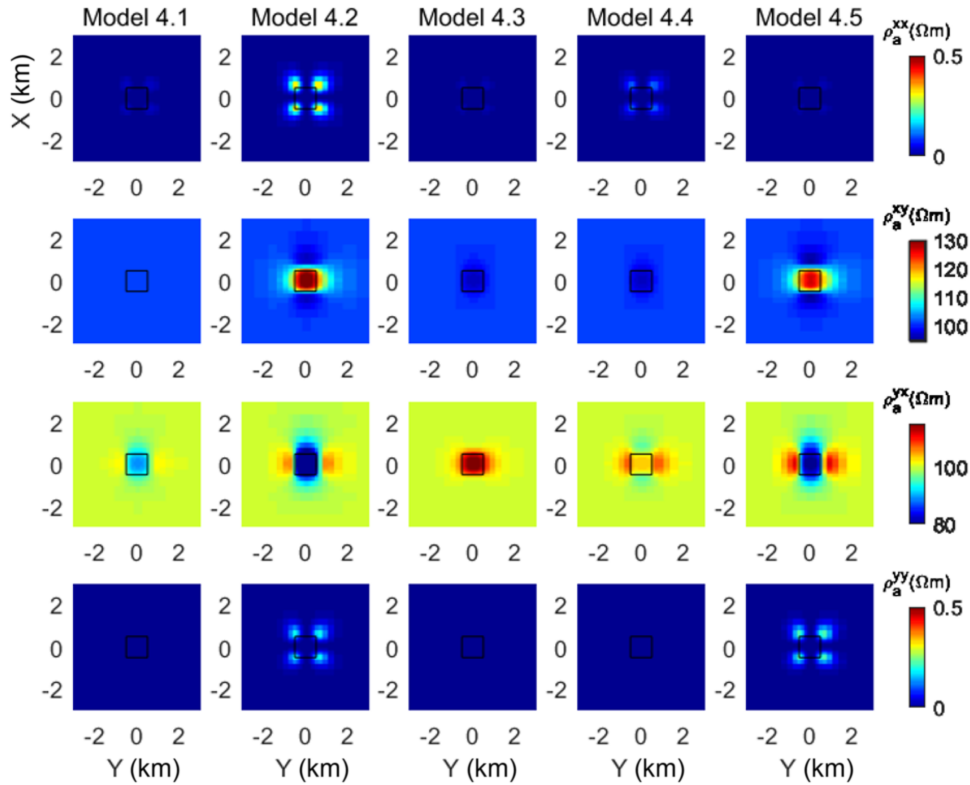
Figure 15 Apparent resistivities of Model 4 at 10 Hz: the first to fourth rows correspond to *xx*-, *xy*-, *yx*- and *yy*-mode apparent resistivities, respectively, whereas the first to third columns correspond to Model 4.1, Model 4.2 and Model 4.3, respectively. Model 4.1 is axial conductive anisotropy, Model 4.2 is axial magnetic anisotropy and Model 4.3 is axial conductive and magnetic anisotropy.

manifested as lower apparent resistivities, whereas the *yx*-mode apparent resistivities manifested as higher apparent resistivities. We also tried to explain these phenomena in a simple axial conductive and magnetic anisotropic half-space: according to (C13) and (C14) in Appendix C, the apparent resistivities can be expressed as $(1 + \chi_{yy})\rho_{xx}$, and $\rho_a^{yx} = (1 + \chi_{xx})\rho_{yy}$; for Model 4.4, the $\rho_a^{yx} = (1 + \chi_{xx})\rho_{yy}$ is 90 Ωm, which is smaller than the background resistivity, and the $\rho_a^{yx} = (1 + \chi_{xx})\rho_{yy}$ is 112 Ωm, which is larger than the background resistivity. (5) Model 4.5 is also axial conductive and magnetic anisotropy. Its axial conductivities are the same as Model 4.2 and its axial magnetic susceptibilities are the same as Model 4.3. Due to the influence of the magnetic susceptibilities, the *xy*-mode apparent resistivities are lower, whereas the *yx*-mode apparent resistivities are higher comparing with the results of Model 4.2. It also can be explained similar to Model 4.4. For an axial conductive and magnetic anisotropic anomaly, it can be concluded that: (1) if $(1 + \chi_{yy})\rho_{xx}$ is larger than background resistivity, the *xy*-mode apparent resistivities will manifested as higher apparent resistivities; (2) if $(1 + \chi_{xx})\rho_{yy}$ is larger than background

resistivity, the *yx*-mode apparent resistivities will manifested as higher apparent resistivities.

6 CONCLUSIONS

We have developed a three-dimensional magnetotelluric (MT) modelling algorithm with the edge-based fine-element method. This algorithm not only takes conductive anisotropy into consideration but also is capable of handling magnetic anisotropy. Comparisons of a non-magnetic case and a magnetic case confirmed the accuracy of this algorithm. The responses of four kinds of models are studied and analysed. Based on the analyses, five main conclusions are safely obtained: (1) for many of the usual MT applications ($\chi < 0.01$) and considering the error associated to real MT data, the susceptibility's effect is not significant. However, for anomalies with high susceptibility and low conductive contrast, the susceptibility's influences cannot be ignored; (2) for magnetic isotropic anomaly, if its magnetic susceptibility is positive, then it will lead to a higher apparent resistivity, and if its magnetic susceptibility is negative, then it will lead to a lower

apparent resistivity; (3) for a lower resistivity anomaly, due to the existence of magnetic susceptibility, its results may manifest as higher apparent resistivities; (4) for a magnetic anisotropic anomaly, if a principal magnetic susceptibility is in the x-direction and keeps unchanged, then the yx-mode apparent resistivities are mainly influenced by this principal magnetic susceptibility, and if a principal magnetic susceptibility is in the y-direction and remains unchanged, then the xy-mode apparent resistivities are mainly influenced by this principal magnetic susceptibility; (5) for an axial conductive and magnetic anisotropic anomaly, if $(1 + \chi_{yy})\rho_{xx}$ is larger (smaller) than background resistivity, the xy-mode apparent resistivities will manifested as higher (lower) apparent resistivities, and if $(1 + \chi_{xx})\rho_{yy}$ is larger (smaller) than background resistivity, the yx-mode apparent resistivities will manifested as higher (lower) apparent resistivities.

ORCID

Tiaojie Xiao https://orcid.org/0000-0002-8378-5530

REFERENCES

Ansari S. and Farquharson C.G. 2014. 3D finite-element forward modeling of electromagnetic data using vector and scalar potentials and unstructured grids. *Geophysics* **79**, E149–E165.

Bardi I. and Biro O. 1991. An efficient finite-element formulation without spurious modes for anisotropic waveguides. *IEEE Transactions on Microwave Theory and Techniques* **39**, 1133–1139.

Biedermann A.R. and McEnroe S.A. 2017. Effects of magnetic anisotropy on total magnetic field anomalies. *Journal of Geophysical Research: Solid Earth* **122**, 8628–8644.

Bolle O., Charlier B., Bascou J., Diot H. and McEnroe S.A. 2014. Anisotropy of magnetic susceptibility versus lattice-and shape-preferred orientation in the lac tio hemo-ilmenite ore body (Grenville province, Quebec). *Tectonophysics* **629**, 87–108.

Cai H., Xiong B., Han M.R. and Michael Z. 2014. 3D controlled-source electromagnetic modeling in anisotropic medium using edge-based finite element method. *Computer & Geosciences* **73**, 164–176.

Cai H., Hu X., Li J., Endo M. and Xiong B. 2017. Parallelized 3D CSEM modeling using edge-based finite element with total field formulation and unstructured mesh. *Computers & Geosciences* **99**, 125–134.

Cao X., Yin C., Zhang B., Huang X., Liu Y. and Cai J. 2018. A goal-oriented adaptive finite-element method for 3D MT anisotropic modeling with topography. *Chinese Journal of Geophysics* **61**, 2618–2628.

Emerson D.W., Clark D.A. and Saul S.J. 1985. Magnetic exploration models incorporating remanence, demagnetization and anisotropy: HP 41C handheld computer algorithms. *Exploration Geophysics* **16**, 1–122.

Everett M.E. 2012. Theoretical developments in electromagnetic induction geophysics with selected applications in the near surface. *Surveys in Geophysics* **33**, 29–63.

Farquharson C.G. and Craven J.A. 2009. Three-dimensional inversion of magnetotelluric data for mineral exploration: an example from the McArthur River uranium deposit, Saskatchewan, Canada. *Journal of Applied Geophysics* **68**, 450–458.

Heinson G.S., Direen N.G. and Gill R.M. 2006. Magnetotelluric evidence for a deep-crustal mineralizing system beneath the Olympic Dam iron oxide copper-gold deposit, southern Australia. *Geology* **34**, 573–576.

Hu X., Peng R., Wu G., Wang W., Huo G. and Han B. 2013. Mineral exploration using CSAMT data: application to Longmen region metallogenic belt, Guangdong Province, China. *Geophysics* **78**, B111–B119.

Hunt C.P., Moskowitz B.M. and Banerjee S.K. 1995. Magnetic properties of rocks and minerals. *Rock Physics and Phase Relations* **3**, 189–204.

Hrouda F. 1982. Magnetic anisotropy of rocks and its application in geology and geophysics. *Geophysical Surveys* **5**, 37–82.

Huo G.P., Hu X.Y., Huang Y.F. and Han B. 2015. MT modeling for two-dimensional anisotropic conductivity structure with topography and examples of comparative analyses. *Chinese Journal of Geophysics* **58**, 4696–4708.

Jin J.M. 2002. *The Finite Element Method in Electromagnetics*, 2nd edn. John Wiley and Sons, New York, NY.

Kao D. and Orr D. 1982. Magnetotelluric response of a uniformly stratified earth containing a magnetized layer. *Geophysical Journal of the Royal Astronomical Society* **70**, 339–347.

Klein K.A. and Santamarina J.C. 2003. Electrical conductivity in soils: underlying phenomena. *Journal of Environmental and Engineering Geophysics* **8**, 263–273.

Kong W., Lin C., Tan H., Peng M., Tong T. and Wang M. 2018. The effects of 3D electrical anisotropy on magnetotelluric responses: synthetic case studies. *Journal of Environmental and Engineering Geophysics* **23**, 61–75.

Kontny A., Engelmann R., Grimmer J.C., Greiling R.O. and Hirt A. 2012. Magnetic fabric development in a highly anisotropic magnetite-bearing ductile shear zone (Seve Nappe Complex, Scandinavian Caledonides). *International Journal of Earth Sciences* **101**, 671–692.

Li J, Farquharson C.G. and Hu X. 2016. 3D vector finite-element electromagnetic forward modeling for large loop sources using a

total-field algorithm and unstructured tetrahedral grids. *Geophysics* **82**, E1–E16.

Li Y. 2000. *Finite element modeling of electromagnetic fields in two- and three-dimensional anisotropic conductivity structures*. PhD thesis, University of Gottingen, Germany.

Li Y. 2002. A finite-element algorithm for electromagnetic induction in two-dimensional anisotropic conductivity structures. *Geophysical Journal International* **148**, 389–401.

Li Y. and Pek J. 2008. Adaptive finite element modelling of two-dimensional magnetotelluric fields in general anisotropic media. *Geophysical Journal International* **175**, 942–954.

Linde N. and Pedersen L.B. 2004. Evidence of electrical anisotropy in limestone formations using the RMT technique. *Geophysics* **69**, 909–916.

Liu Y., Xu Z. and Li Y. 2018. Adaptive finite element modelling of three-dimensional magnetotelluric fields in general anisotropic media. *Journal of Applied Geophysics* **151**, 113–124.

Løseth L.O. and Ursin B. 2007. Electromagnetic fields in planarly layered anisotropic media. *Geophysical Journal International* **170**, 44–80.

Marin L.E., Steinich B., Jaglowski D. and Barcelona M.J. 1998. Hydrogeologic site characterization using azimuthal resistivity surveys. *Journal of Environmental and Engineering Geophysics* **3**, 179–184.

Martí A. 2014. The role of electrical anisotropy in magnetotelluric responses: from modelling and dimensionality analysis to inversion and interpretation. *Surveys in Geophysics* **35**, 179–218.

Martinelli P. and Osella A. 1997. MT forward modeling of 3-D anisotropic electrical conductivity structures using the Rayleigh-Fourier method. *Journal of Geomagnetism and Geoelectricity* **49**, 1499–1518.

Mitsuhata Y., Matsuo K. and Minegishi M. 1999. Magnetotelluric survey for exploration of a volcanic-rock reservoir in the Yurihara oil and gas field, Japan. *Geophysical Prospecting* **47**, 195–218.

Mukherjee S. and Everett M.E. 2011. 3D controlled-source electromagnetic edge-based finite element modeling of conductive and permeable heterogeneities. *Geophysics* **76**, F215–F226.

Noh K., Oh S., Seol S.J., Lee K.H. and Byun J. 2016. Analysis of anomalous electrical conductivity and magnetic permeability effects using a frequency domain controlled-source electromagnetic method. *Geophysical Journal International* **204**, 1550–1564.

O'Brien D.P. and Morrison H.F. 1967. Electromagnetic fields in an N-layered anisotropic half-space. *Geophysics* **32**, 668–677.

Pek J. and Santos F.A. 2002. Magnetotelluric impedances and parametric sensitivities for 1-D anisotropic layered media. *Computers and Geosciences* **28**, 939–950.

Pek J. and Verner T. 1997. Finite-difference modelling of magnetotelluric fields in two-dimensional anisotropic media. *Geophysical Journal International* **128**, 505–521.

Reddy I.K. and Rankin D. 1971. Magnetotelluric effect of dipping anisotropies. *Geophysical Prospecting* **19**, 84–97.

Ren Z.Y., Kalscheuer T., Greenhalgh S. and Maurer H. 2013. A goal-oriented adaptive finite-element approach for plane wave 3-D electromagnetic modeling. *Geophysical Journal International* **194**, 700–718.

Ren Z.Y., Kalscheuer T, Greenhalgh S. and Maurer H. 2014. A finite-element-based domain-decomposition approach for plane wave 3D electromagnetic modeling. *Geophysics* **79**, E255–E268.

Rochette P., Jackson M. and Aubourg C. 1992. Rock magnetism and the interpretation of anisotropy of magnetic susceptibility. *Reviews of Geophysics* **30**, 209–226.

Sasaki Y., Kim J.H. and Cho S.J. 2010. Multidimensional inversion of loop-loop frequency-domain EM data for resistivity and magnetic susceptibility. *Geophysics* **75**, 907–917.

Spichak V., Geiermann J., Zakharova O., Calcagno P., Genter A. and Schill E. 2015. Estimating deep temperatures in the soultz-sous-forêts geothermal area (France) from magnetotelluric data. *Near Surface Geophysics* **13**, 397–408.

Starostenko V.I., Shuman V.N., Ivashchenko I.N., Legostaeva O.V., Savchenko A.S. and Skrinik O.Y. 2009. Magnetic fields of 3-D anisotropic bodies: theory and practice of calculations. *Izvestiya Physics of the Solid Earth* **45**, 640–655.

Unsworth M., Bedrosian P., Eisel M., Egbert G. and Siripunvaraporn W. 2000. Along strike variations in the electrical structure of the San Andreas Fault at Parkfield, California. *Geophysical Research Letters* **27**, 3021–3024.

Villain G., Ihamouten A., du Plooy R., Lopes S.P. and Derobert X. 2015. Use of electromagnetic non-destructive techniques for monitoring water and chloride ingress into concrete. *Near Surface Geophysics* **13**, 299–309.

Wang K. and Tan H. 2017. Research on the forward modeling of controlled-source audio-frequency magnetotellurics in three-dimensional axial anisotropic media. *Journal of Applied Geophysics* **146**, 27–36.

Wang K., Tan H., Zhang Z., Li Z. and Cao M. 2016. Divergence correction schemes in finite difference method for 3D tensor CSAMT in axial anisotropic media. *Exploration Geophysics* **48**, 363–373.

Wannamaker P.E. 2005. Anisotropy versus heterogeneity in continental solid earth electromagnetic studies: fundamental response characteristics and implications for physicochemical state. *Surveys in Geophysics* **26**, 733–765.

Weidelt P., Oristaglio M. and Spies B. 1999. 3-D conductivity models: implications of electrical anisotropy. *Three-Dimensional Electromagnetics* **7**, 119–137.

Xiao T., Liu Y., Wang Y. and Fu L.Y. 2018. Three-dimensional magnetotelluric modeling in anisotropic media using edge-based finite element method. *Journal of Applied Geophysics* **149**, 1–9.

Xu S.Z. 1994. *The Finite Element Methods in Geophysics*. Science Press, Beijing, China.

Yadav G.S. and Lal T. 1997. A fortran 77 program for computing magnetotelluric response over a stratified earth with changing magnetic permeability. *Computers and Geosciences* **23**, 1035–1038.

Yin C. 2000. Geoelectrical inversion for a one-dimensional anisotropic model and inherent non-uniqueness. *Geophysical Journal International* **140**, 11–23.

Yin C. 2003. Inherent nonuniqueness in magnetotelluric inversion for 1D anisotropic models. *Geophysics* **68**, 138–146.

Yin C. 2006. MMT forward modeling for a layered earth with arbitrary anisotropy. *Geophysics* **71**, G115–G128.

Zhang Z. and Oldenburg D.W. 1997. Recovering magnetic suscep-
tibility from electromagnetic data over a one-dimensional earth.
Geophysical Journal International **130**, 422–434.

Zhdanov M.S. and Pavlov D.A. 2001. Analysis and interpretation
of anomalous conductivity and magnetic permeability effects in
time domain electromagnetic data: part ii: sμ -inversion. *Journal of
Applied Geophysics* **46**, 217–233.

APPENDIX A: THE VALUES OF $\mathbf{K}_{1e}$ AND $\mathbf{K}_{2e}$

$\tilde{v}$ is the magnetic reluctivity tensor, it can be expressed as
follows:

$$\tilde{v} = \begin{bmatrix} v_{xx} & v_{xy} & v_{xz} \\ v_{yx} & v_{yy} & v_{yz} \\ v_{zx} & v_{zy} & v_{zz} \end{bmatrix}, \tag{A1}$$

a, b and c are side lengths of the hexahedral element (as shown
in Fig. 2) in the x-, y-, and z-direction, respectively.

1. $\mathbf{K}_{1e}$ of equation (16)

$$\mathbf{K}_{1e} = \begin{bmatrix} 0 & \frac{\partial \mathbf{N}_x^e}{\partial z} & -\frac{\partial \mathbf{N}_x^e}{\partial y} \\ -\frac{\partial \mathbf{N}_y^e}{\partial z} & 0 & \frac{\partial \mathbf{N}_y^e}{\partial x} \\ \frac{\partial \mathbf{N}_z^e}{\partial y} & -\frac{\partial \mathbf{N}_z^e}{\partial x} & 0 \end{bmatrix} \begin{bmatrix} v_{xx} & v_{xy} & v_{xz} \\ v_{yx} & v_{yy} & v_{yz} \\ v_{zx} & v_{zy} & v_{zz} \end{bmatrix}$$

$$\times \begin{bmatrix} 0 & -\left(\frac{\partial \mathbf{N}_y^e}{\partial z}\right)^T & \left(\frac{\partial \mathbf{N}_z^e}{\partial y}\right)^T \\ \left(\frac{\partial \mathbf{N}_x^e}{\partial z}\right)^T & 0 & -\left(\frac{\partial \mathbf{N}_z^e}{\partial x}\right)^T \\ -\left(\frac{\partial \mathbf{N}_x^e}{\partial y}\right)^T & \left(\frac{\partial \mathbf{N}_y^e}{\partial x}\right)^T & 0 \end{bmatrix}$$

$$= \begin{bmatrix} \mathbf{K}_{1e}^{xx} & \mathbf{K}_{1e}^{xy} & \mathbf{K}_{1e}^{xz} \\ \mathbf{K}_{1e}^{yx} & \mathbf{K}_{1e}^{yy} & \mathbf{K}_{1e}^{yz} \\ \mathbf{K}_{1e}^{zx} & \mathbf{K}_{1e}^{zy} & \mathbf{K}_{1e}^{zz} \end{bmatrix}, \tag{A2}$$

where

$$K_{1e}^{xx} = v_{yy}\frac{ab}{6c}\begin{bmatrix} 2 & 1 & -2 & -1 \\ 1 & 2 & -1 & -2 \\ -2 & -1 & 2 & 1 \\ -1 & -2 & 1 & 2 \end{bmatrix}$$

$$+ v_{zy}\frac{a}{4}\begin{bmatrix} -1 & -1 & 1 & 1 \\ 1 & 1 & -1 & -1 \\ -1 & -1 & 1 & 1 \\ 1 & 1 & -1 & -1 \end{bmatrix}$$

$$+ v_{yz}\frac{a}{4}\begin{bmatrix} -1 & 1 & -1 & 1 \\ -1 & 1 & -1 & 1 \\ 1 & -1 & 1 & -1 \\ 1 & -1 & 1 & -1 \end{bmatrix}$$

$$+ v_{zz}\frac{ac}{6b}\begin{bmatrix} 2 & -2 & 1 & -1 \\ -2 & 2 & -1 & 1 \\ 1 & -1 & 2 & -2 \\ -1 & 1 & -2 & 2 \end{bmatrix}, \tag{A3}$$

$$K_{1e}^{yx} = v_{xy}\frac{ab}{4c}\begin{bmatrix} -1 & -1 & 1 & 1 \\ 1 & 1 & -1 & -1 \\ -1 & -1 & 1 & 1 \\ 1 & 1 & -1 & -1 \end{bmatrix}$$

$$+ v_{zy}\frac{b}{4}\begin{bmatrix} 1 & 1 & -1 & -1 \\ 1 & 1 & -1 & -1 \\ -1 & -1 & 1 & 1 \\ -1 & -1 & 1 & 1 \end{bmatrix}$$

$$+ v_{xz}\frac{a}{4}\begin{bmatrix} 1 & -1 & 1 & -1 \\ -1 & 1 & -1 & 1 \\ 1 & -1 & 1 & -1 \\ -1 & 1 & -1 & 1 \end{bmatrix}$$

$$+ v_{zz}\frac{c}{6}\begin{bmatrix} -2 & 2 & -1 & 1 \\ -1 & 1 & -2 & 2 \\ 2 & -2 & 1 & -1 \\ 1 & -1 & 2 & -2 \end{bmatrix}, \tag{A4}$$

$$K_{1e}^{zx} = v_{xy}\frac{a}{4}\begin{bmatrix} 1 & 1 & -1 & -1 \\ 1 & 1 & -1 & -1 \\ -1 & -1 & 1 & 1 \\ -1 & -1 & 1 & 1 \end{bmatrix}$$

$$+ v_{yy}\frac{b}{6}\begin{bmatrix} -2 & -1 & 2 & 1 \\ 2 & 1 & -2 & -1 \\ -1 & -2 & 1 & 2 \\ 1 & 2 & -1 & -2 \end{bmatrix}$$

$$+ v_{xz}\frac{ac}{4b}\begin{bmatrix} -1 & 1 & -1 & 1 \\ -1 & 1 & -1 & 1 \\ 1 & -1 & 1 & -1 \\ 1 & -1 & 1 & -1 \end{bmatrix}$$

$$+ v_{yz}\frac{c}{4}\begin{bmatrix} 1 & -1 & 1 & -1 \\ -1 & 1 & -1 & 1 \\ 1 & -1 & 1 & -1 \\ -1 & 1 & -1 & 1 \end{bmatrix}, \tag{A5}$$

$$+ v_{xz}\frac{b}{4}\begin{bmatrix} -1 & -1 & 1 & 1 \\ 1 & 1 & -1 & -1 \\ -1 & -1 & 1 & 1 \\ 1 & 1 & -1 & -1 \end{bmatrix}$$

$$+ v_{zz}\frac{bc}{6a}\begin{bmatrix} 2 & 1 & -2 & -1 \\ 1 & 2 & -1 & -2 \\ -2 & -1 & 2 & 1 \\ -1 & -2 & 1 & 2 \end{bmatrix}, \tag{A7}$$

$$K_{1e}^{xy} = v_{yx}\frac{ab}{4c}\begin{bmatrix} -1 & 1 & -1 & 1 \\ -1 & 1 & -1 & 1 \\ 1 & -1 & 1 & -1 \\ 1 & -1 & 1 & -1 \end{bmatrix}$$

$$+ v_{zx}\frac{a}{4}\begin{bmatrix} 1 & -1 & 1 & -1 \\ -1 & 1 & -1 & 1 \\ 1 & -1 & 1 & -1 \\ -1 & 1 & -1 & 1 \end{bmatrix}$$

$$+ v_{yz}\frac{b}{4}\begin{bmatrix} 1 & 1 & -1 & -1 \\ 1 & 1 & -1 & -1 \\ -1 & -1 & 1 & 1 \\ -1 & -1 & 1 & 1 \end{bmatrix}$$

$$+ v_{zz}\frac{c}{6}\begin{bmatrix} -2 & -1 & 2 & 1 \\ 2 & 1 & -2 & -1 \\ -1 & -2 & 1 & 2 \\ 1 & 2 & -1 & -2 \end{bmatrix}, \tag{A6}$$

$$K_{1e}^{zy} = v_{xx}\frac{a}{6}\begin{bmatrix} -2 & 2 & -1 & 1 \\ -1 & 1 & -2 & 2 \\ 2 & -2 & 1 & -1 \\ 1 & -1 & 2 & -2 \end{bmatrix}$$

$$+ v_{yx}\frac{b}{4}\begin{bmatrix} 1 & -1 & 1 & -1 \\ -1 & 1 & -1 & 1 \\ 1 & -1 & 1 & -1 \\ -1 & 1 & -1 & 1 \end{bmatrix}$$

$$+ v_{xz}\frac{c}{4}\begin{bmatrix} 1 & 1 & -1 & -1 \\ 1 & 1 & -1 & -1 \\ -1 & -1 & 1 & 1 \\ -1 & -1 & 1 & 1 \end{bmatrix}$$

$$+ v_{yz}\frac{bc}{4a}\begin{bmatrix} -1 & -1 & 1 & 1 \\ 1 & 1 & -1 & -1 \\ -1 & -1 & 1 & 1 \\ 1 & 1 & -1 & -1 \end{bmatrix}, \tag{A8}$$

$$K_{1e}^{yy} = v_{xx}\frac{ab}{6c}\begin{bmatrix} 2 & -2 & 1 & -1 \\ -2 & 2 & -1 & 1 \\ 1 & -1 & 2 & -2 \\ -1 & 1 & -2 & 2 \end{bmatrix}$$

$$+ v_{zx}\frac{b}{4}\begin{bmatrix} -1 & 1 & -1 & 1 \\ -1 & 1 & -1 & 1 \\ 1 & -1 & 1 & -1 \\ 1 & -1 & 1 & -1 \end{bmatrix}$$

$$K_{1e}^{xz} = v_{yx}\frac{a}{4}\begin{bmatrix} 1 & 1 & -1 & -1 \\ 1 & 1 & -1 & -1 \\ -1 & -1 & 1 & 1 \\ -1 & -1 & 1 & 1 \end{bmatrix}$$

$$+ v_{zx}\frac{ac}{4b}\begin{bmatrix} -1 & -1 & 1 & 1 \\ 1 & 1 & -1 & -1 \\ -1 & -1 & 1 & 1 \\ 1 & 1 & -1 & -1 \end{bmatrix}$$

$$+ v_{yy}\frac{b}{6}\begin{bmatrix} -2 & 2 & -1 & 1 \\ -1 & 1 & -2 & 2 \\ 2 & -2 & 1 & -1 \\ 1 & -1 & 2 & -2 \end{bmatrix}$$

$$+ v_{zy}\frac{c}{4}\begin{bmatrix} 1 & -1 & 1 & -1 \\ -1 & 1 & -1 & 1 \\ 1 & -1 & 1 & -1 \\ -1 & 1 & -1 & 1 \end{bmatrix}, \tag{A9}$$

$$K_{1e}^{yz} = v_{xx}\frac{a}{6}\begin{bmatrix} -2 & -1 & 2 & 1 \\ 2 & 1 & -2 & -1 \\ -1 & -2 & 1 & 1 \\ 1 & 2 & -1 & -2 \end{bmatrix}$$

$$+ v_{zx}\frac{c}{4}\begin{bmatrix} 1 & 1 & -1 & -1 \\ 1 & 1 & -1 & -1 \\ -1 & -1 & 1 & 1 \\ -1 & -1 & 1 & 1 \end{bmatrix}$$

$$+ v_{xy}\frac{b}{4}\begin{bmatrix} 1 & -1 & 1 & -1 \\ -1 & 1 & -1 & 1 \\ 1 & -1 & 1 & -1 \\ -1 & 1 & -1 & 1 \end{bmatrix}$$

$$+ v_{zy}\frac{bc}{4a}\begin{bmatrix} -1 & 1 & -1 & 1 \\ -1 & 1 & -1 & 1 \\ 1 & -1 & 1 & -1 \\ 1 & -1 & 1 & -1 \end{bmatrix}, \tag{A10}$$

$$K_{1e}^{zz} = v_{xx}\frac{ac}{6b}\begin{bmatrix} 2 & 1 & -2 & -1 \\ 1 & 2 & -1 & -2 \\ -2 & -1 & 2 & 1 \\ -1 & -2 & 1 & 2 \end{bmatrix}$$

$$+ v_{yx}\frac{c}{4}\begin{bmatrix} -1 & -1 & 1 & 1 \\ 1 & 1 & -1 & -1 \\ -1 & -1 & 1 & 1 \\ 1 & 1 & -1 & -1 \end{bmatrix}$$

$$+ v_{xy}\frac{c}{4}\begin{bmatrix} -1 & 1 & -1 & 1 \\ -1 & 1 & -1 & 1 \\ 1 & -1 & 1 & -1 \\ 1 & -1 & 1 & -1 \end{bmatrix}$$

$$+ v_{yy}\frac{bc}{6a}\begin{bmatrix} 2 & -2 & 1 & -1 \\ -2 & 2 & -1 & 1 \\ 1 & -1 & 2 & -2 \\ -1 & 1 & -2 & 2 \end{bmatrix}. \tag{A11}$$

2. $\mathbf{K}_{2e}$ of equation (18)

$$\mathbf{K}_{2e} = -i\omega\mu\begin{bmatrix} \mathbf{N}_x^e & 0 & 0 \\ 0 & \mathbf{N}_y^e & 0 \\ 0 & 0 & \mathbf{N}_z^e \end{bmatrix}\begin{bmatrix} \sigma_{xx} & \sigma_{xy} & \sigma_{xz} \\ \sigma_{yx} & \sigma_{yy} & \sigma_{yz} \\ \sigma_{zx} & \sigma_{zy} & \sigma_{zz} \end{bmatrix}$$

$$\times\begin{bmatrix} (\mathbf{N}_x^e)^T & 0 & 0 \\ 0 & (\mathbf{N}_y^e)^T & 0 \\ 0 & 0 & (\mathbf{N}_z^e)^T \end{bmatrix}$$

$$= \begin{bmatrix} \sigma_{xx}\mathbf{K}_{2e}^{xx} & \sigma_{xy}\mathbf{K}_{2e}^{xy} & \sigma_{xz}\mathbf{K}_{2e}^{xz} \\ \sigma_{yx}\mathbf{K}_{2e}^{yx} & \sigma_{yy}\mathbf{K}_{2e}^{yy} & \sigma_{yz}\mathbf{K}_{2e}^{yz} \\ \sigma_{zx}\mathbf{K}_{2e}^{zx} & \sigma_{zy}\mathbf{K}_{2e}^{zy} & \sigma_{zz}\mathbf{K}_{2e}^{zz} \end{bmatrix}, \tag{A12}$$

$$\mathbf{K}_{2e}^{xx} = \mathbf{K}_{2e}^{xy} = \mathbf{K}_{2e}^{xz} = \mathbf{K}_{2e}^{yx} = \mathbf{K}_{2e}^{yy} = \mathbf{K}_{2e}^{yz} = \mathbf{K}_{2e}^{zx} = \mathbf{K}_{2e}^{zy} = \mathbf{K}_{2e}^{zz}$$

$$= -i\omega(k_{ij})_{4\times 4} = -i\omega(N_{xi}N_{xj})_{4\times 4}$$

$$= -i\omega\frac{abc}{36}\begin{bmatrix} 4 & 2 & 2 & 1 \\ 2 & 4 & 1 & 2 \\ 2 & 1 & 4 & 2 \\ 1 & 2 & 2 & 4 \end{bmatrix}. \tag{A13}$$

APPENDIX B

1. The results of Model 1: the apparent resistivities and phases
of Model 1 are shown in this section.
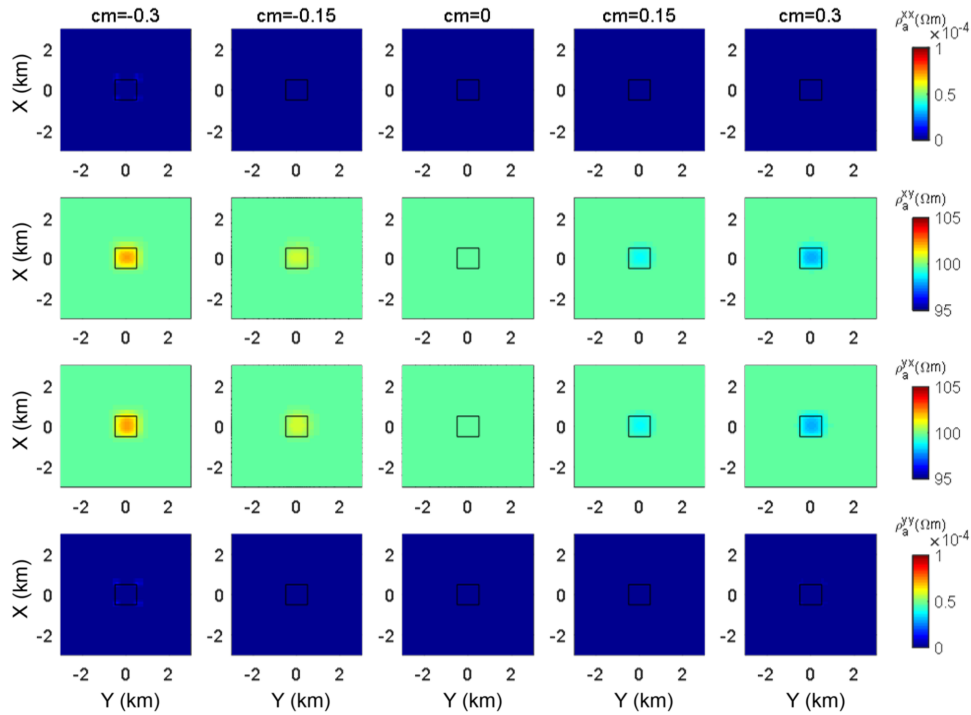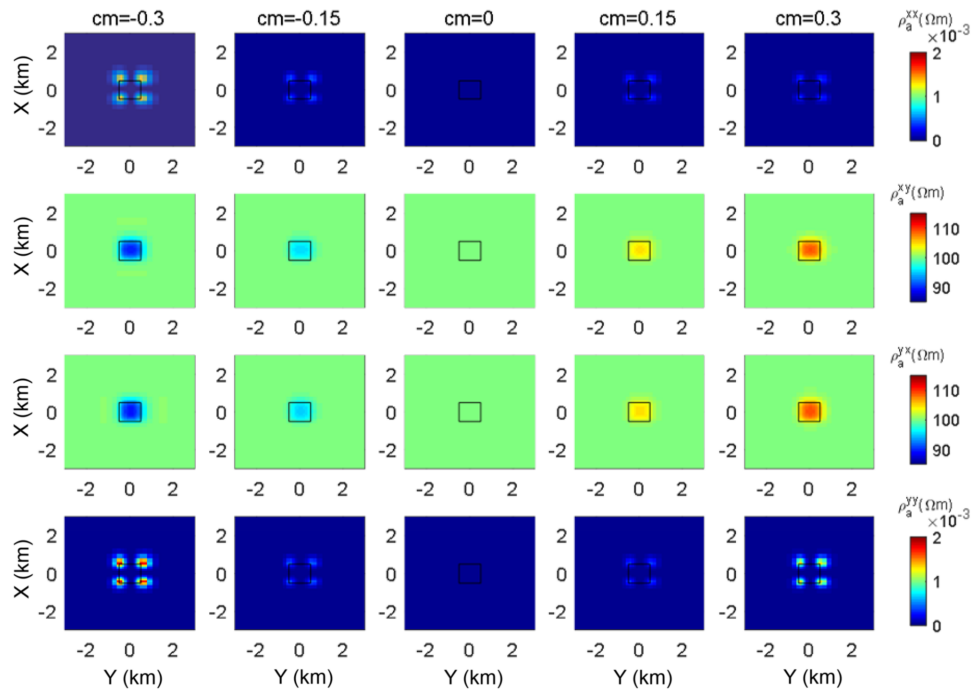
2. The apparent resistivities of Model 2.2:

Figure B1 Apparent resistivities of Model 1 with different magnetic susceptibilities at 1000 Hz: the first to fourth rows correspond to the apparent resistivities of *xx*-, *xy*-, *yx*- and *yy*-mode, respectively; the first to fifth columns correspond to magnetic susceptibilities of –0.3, –0.15, 0, 0.15 and 0.3, respectively. The black square represents the 3D anomaly.
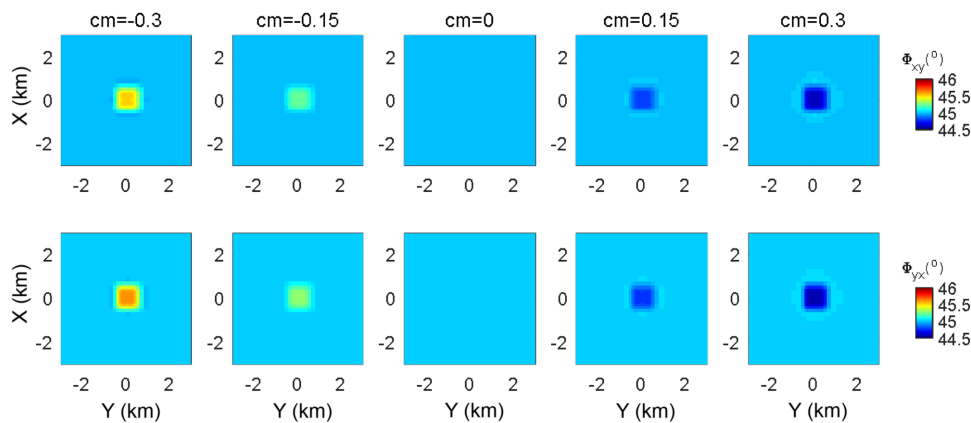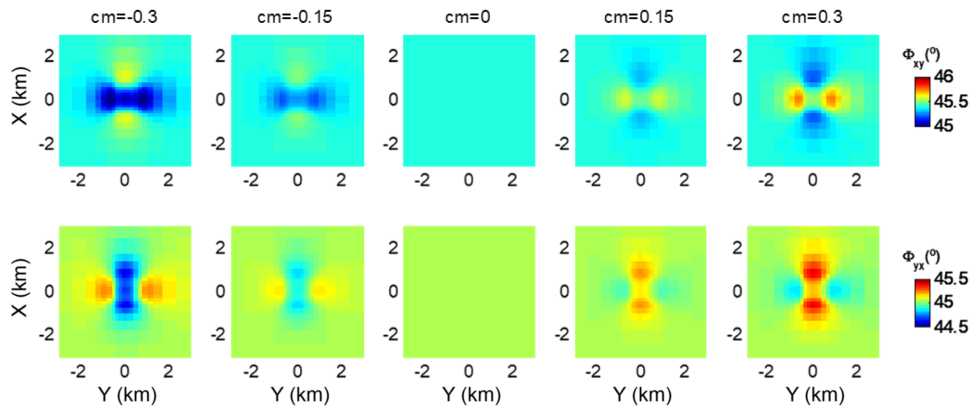

Figure B2 Phases of Model 1 with different magnetic susceptibilities at 1000 Hz: the upper row and the lower row correspond to *xy*- and *yx*-mode, respectively; the first to fifth columns correspond to magnetic susceptibilities of –0.3, –0.15, 0, 0.15 and 0.3, respectively.
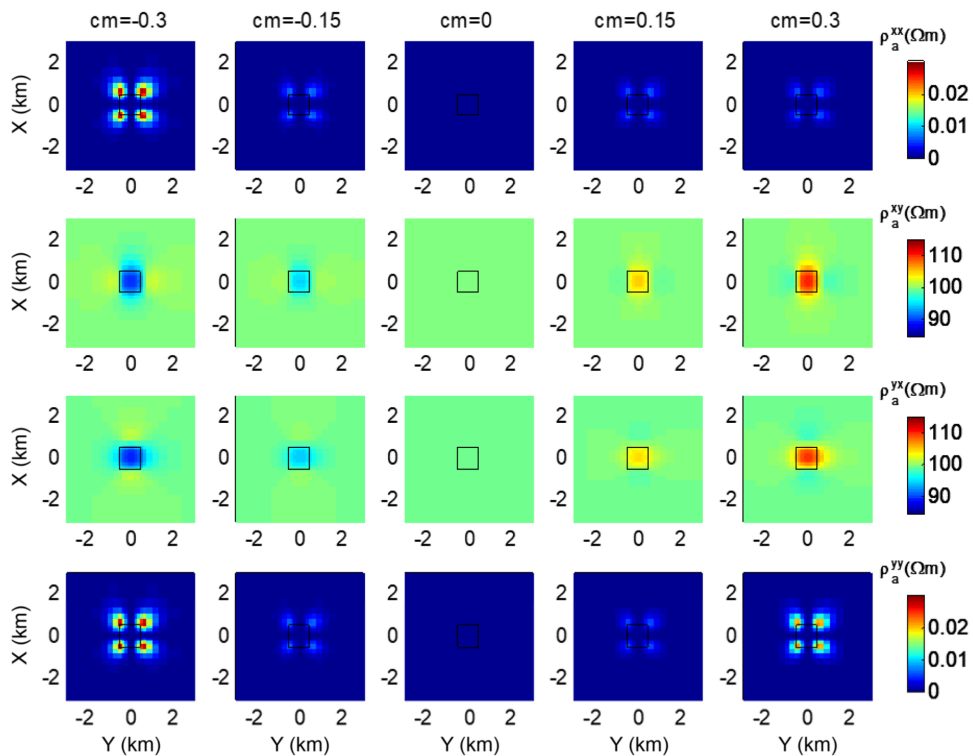
Figure B3 Apparent resistivities of Model 1 with different magnetic susceptibilities at 100 Hz: the first to fourth rows correspond to the apparent resistivities of *xx*-, *xy*-, *yx*- and *yy*-mode, respectively; the first to fifth columns correspond to magnetic susceptibilities of –0.3, –0.15, 0, 0.15 and 0.3, respectively. The black square represents the 3D anomaly.
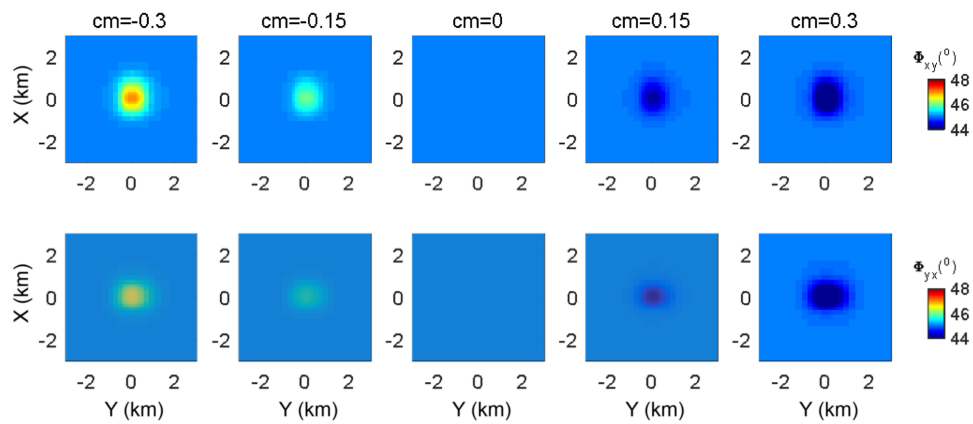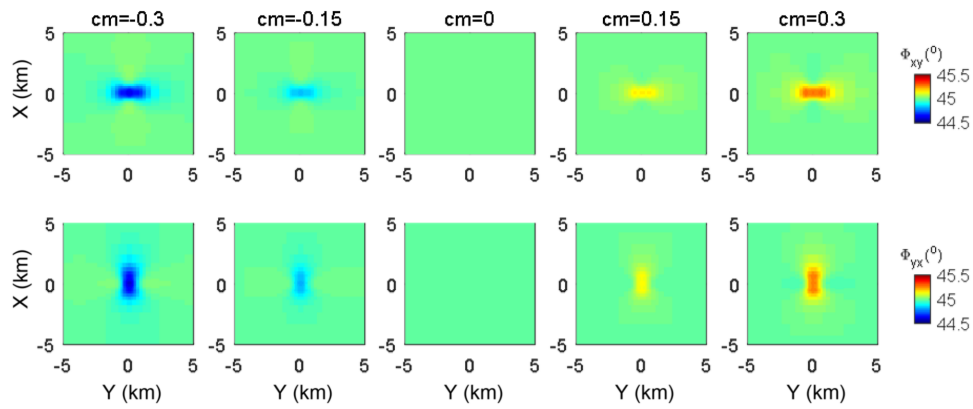

Figure B4 Phases of Model 1 with different magnetic susceptibilities at 100 Hz: the upper row and the lower row correspond to *xy*- and *yx*-mode, respectively; the first to fifth columns correspond to magnetic susceptibilities of –0.3, –0.15, 0, 0.15 and 0.3, respectively.

Figure B5 Phases of Model 1 with different magnetic susceptibilities at 10 Hz: the upper row and the lower row correspond to *xy*- and *yx*-mode, respectively; the first to fifth columns correspond to magnetic susceptibilities of –0.3, –0.15, 0, 0.15 and 0.3, respectively.
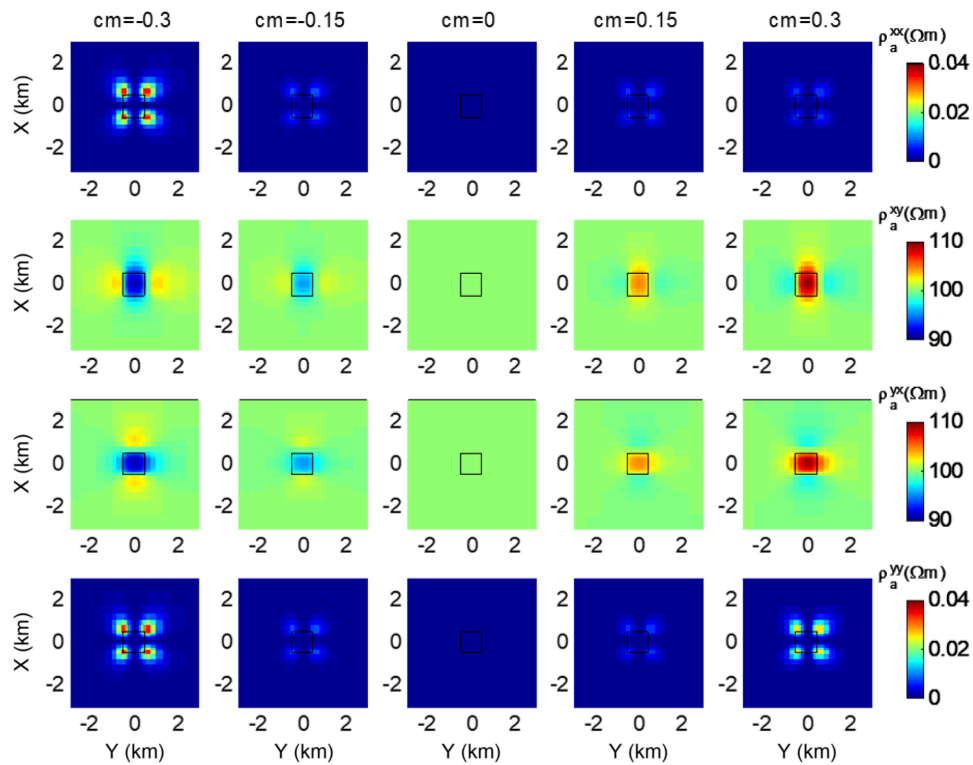

Figure B6 Apparent resistivities of Model 1 with different magnetic susceptibilities at 1 Hz: the first to fourth rows correspond to the apparent resistivities of *xx*-, *xy*-, *yx*- and *yy*-mode, respectively; the first to fifth columns correspond to magnetic susceptibilities of –0.3, –0.15, 0, 0.15 and 0.3, respectively. The black square represents the 3D anomaly.
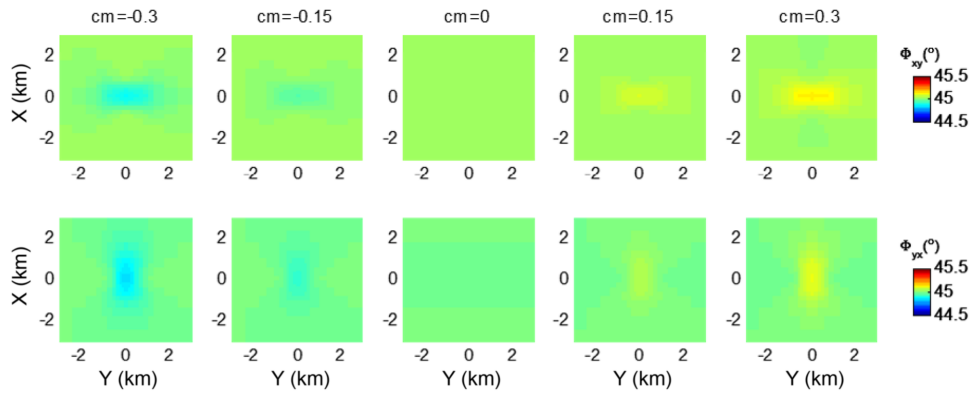
Figure B7 Phases of Model 1 with different magnetic susceptibilities at 1 Hz: the upper row and the lower row correspond to *xy*- and *yx*-mode, respectively; the first to fifth columns correspond to magnetic susceptibilities of –0.3, –0.15, 0, 0.15 and 0.3, respectively.
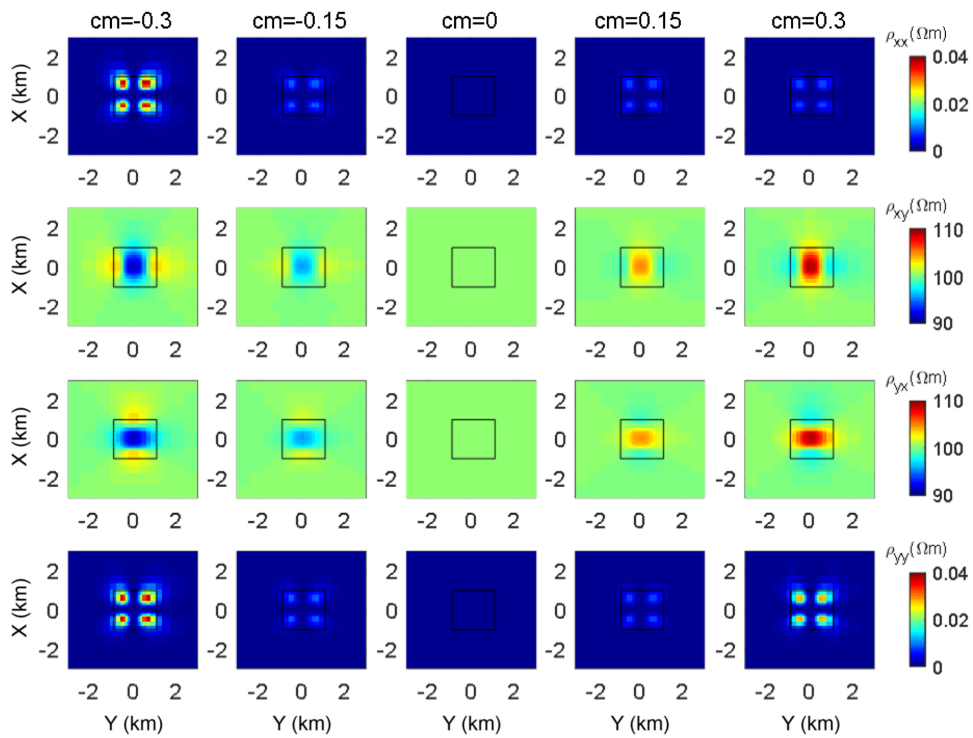

Figure B8 Apparent resistivities of Model 1 with different magnetic susceptibilities at 0.1 Hz: the first to fourth rows correspond to the apparent resistivities of *xx*-, *xy*-, *yx*- and *yy*-mode, respectively; the first to fifth columns correspond to magnetic susceptibilities of –0.3, –0.15, 0, 0.15 and 0.3, respectively. The black square represents the 3D anomaly.

Figure B9 Phases of Model 1 with different magnetic susceptibilities at 0.1 Hz: the upper row and the lower row correspond to *xy*- and *yx*-mode, respectively; the first to fifth columns correspond to magnetic susceptibilities of –0.3, –0.15, 0, 0.15 and 0.3, respectively.

Figure B10 Apparent resistivities of Model 1 with different magnetic susceptibilities at 0.01 Hz: the first to fourth rows correspond to the apparent resistivities of *xx*-, *xy*-, *yx*- and *yy*-mode, respectively; the first to fifth columns correspond to magnetic susceptibilities of –0.3, –0.15, 0, 0.15 and 0.3, respectively. The black square represents the 3D anomaly.
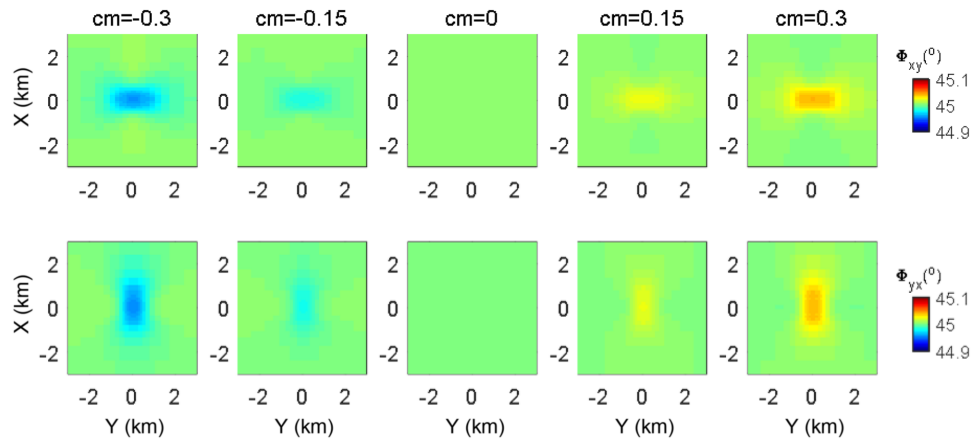
Figure B11 Phases of Model 1 with different magnetic susceptibilities at 0.01 Hz: the upper row and the lower row correspond to *xy-* and *yx*-mode, respectively; the first to fifth columns correspond to magnetic susceptibilities of –0.3, –0.15, 0, 0.15 and 0.3, respectively.
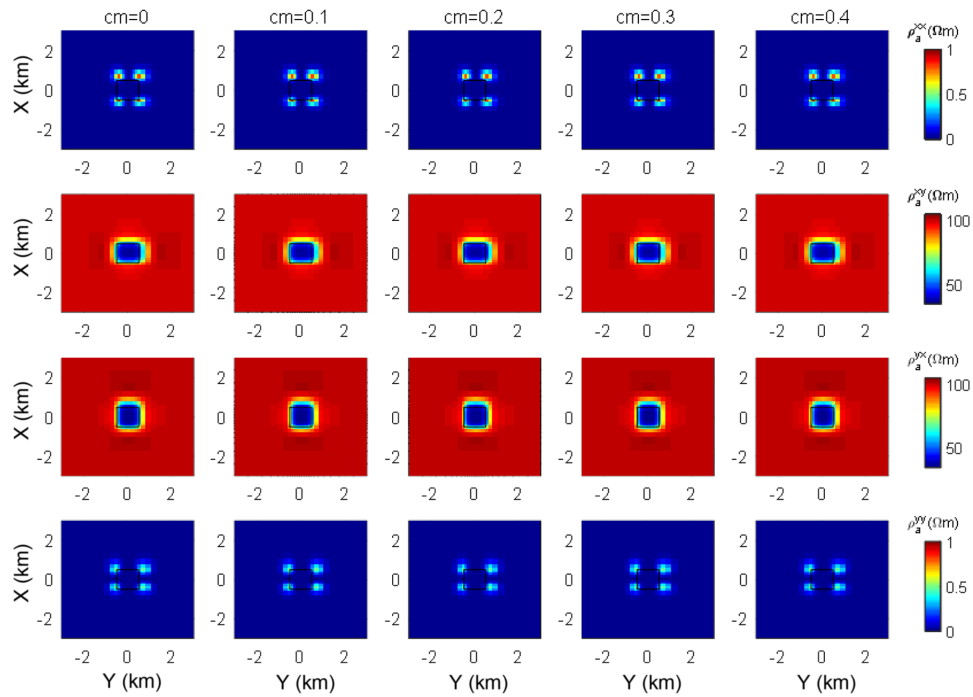

Figure B12 Apparent resistivities of Model 2.2 with different magnetic susceptibilities at 100 Hz: the first to fourth rows correspond to the apparent resistivities of *xx-*, *xy-*, *yx-* and *yy*-mode, respectively; the first to fifth columns correspond to magnetic susceptibilities of –0.3, –0.15, 0, 0.15 and 0.3, respectively. The black square represents the 3D anomaly.
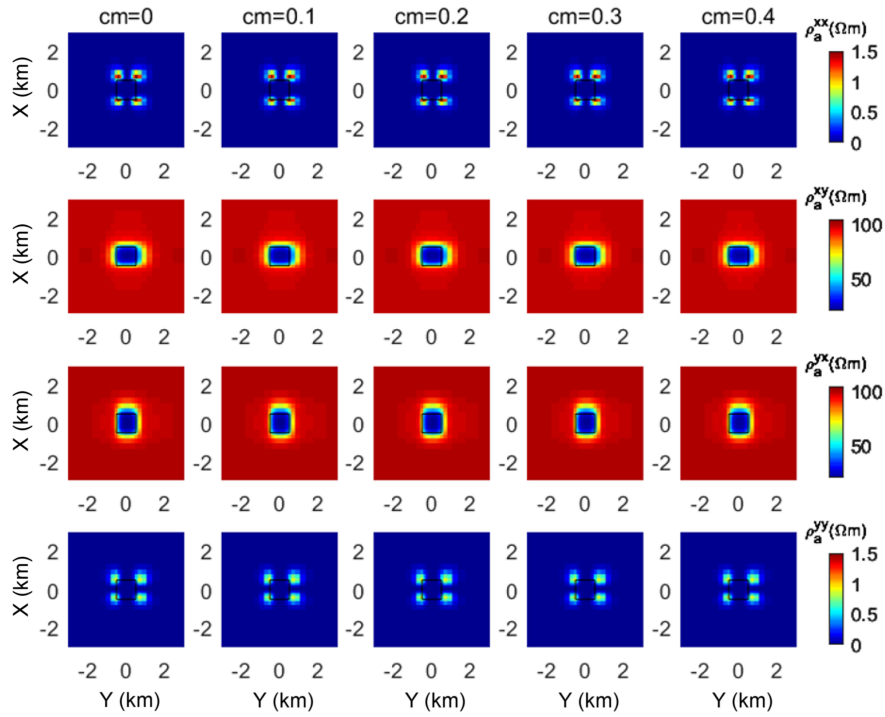
Figure B13 Apparent resistivities of Model 2.2 with different magnetic susceptibilities at 50 Hz: the first to fourth rows correspond to the apparent resistivities of *xx*-, *xy*-, *yx*- and *yy*-mode, respectively; the first to fifth columns correspond to magnetic susceptibilities of –0.3, –0.15, 0, 0.15 and 0.3, respectively. The black square represents the 3D anomaly.
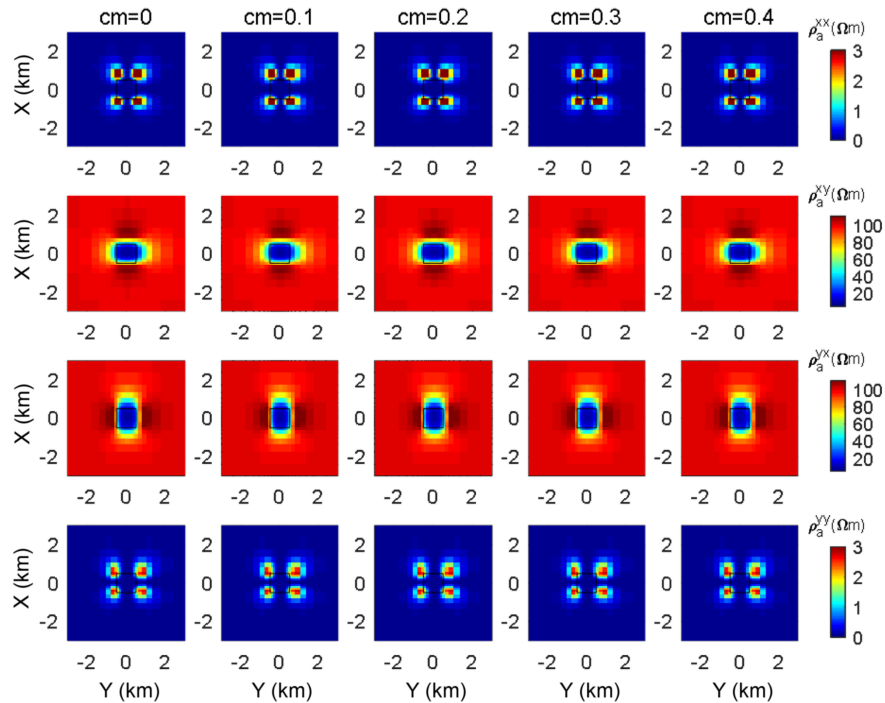

Figure B14 Apparent resistivities of Model 2.2 with different magnetic susceptibilities at 10 Hz: the first to fourth rows correspond to the apparent resistivities of *xx*-, *xy*-, *yx*- and *yy*-mode, respectively; the first to fifth columns correspond to magnetic susceptibilities of –0.3, –0.15, 0, 0.15 and 0.3, respectively. The black square represents the 3D anomaly.

APPENDIX C

In this section, the apparent resistivities in axial conductive and magnetic anisotropic media have been derived. In conductive and magnetic anisotropic media, (C1) and (C2) can be obtained according to the Maxwell's equations:

$$\nabla \times \mathbf{E} = i\omega\mu_0 \begin{bmatrix} 1+\chi_{xx} & \chi_{xy} & \chi_{xz} \\ \chi_{yx} & 1+\chi_{yy} & \chi_{yz} \\ \chi_{zx} & \chi_{zy} & 1+\chi_{zz} \end{bmatrix} \mathbf{H}, \tag{C1}$$

$$\nabla \times \mathbf{H} = \begin{bmatrix} \sigma_{xx} & \sigma_{xy} & \sigma_{xz} \\ \sigma_{yx} & \sigma_{yy} & \sigma_{yz} \\ \sigma_{zx} & \sigma_{zy} & \sigma_{zz} \end{bmatrix} \mathbf{E}. \tag{C2}$$

The symbols used here are consistent with the symbols in the text. For an axial conductive and magnetic half-space, equations (C3)–(C8) can be obtained from (C1) and (C2),

$$-\frac{\partial \mathbf{E}_y}{\partial z} = i\omega\mu_0(1+\chi_{xx})\mathbf{H}_x, \tag{C3}$$

$$\frac{\partial \mathbf{E}_x}{\partial z} = i\omega\mu_0(1+\chi_{yy})\mathbf{H}_y, \tag{C4}$$

$$\mathbf{H}_z = 0, \tag{C5}$$

$$-\frac{\partial \mathbf{H}_y}{\partial z} = \sigma_{xx}\mathbf{E}_x, \tag{C6}$$

$$\frac{\partial \mathbf{H}_x}{\partial z} = \sigma_{yy}\mathbf{E}_y, \tag{C7}$$

$$\mathbf{E}_z = 0. \tag{C8}$$

For Source A: $\mathbf{E}_A = (\mathbf{E}_A^x, \mathbf{E}_A^y, \mathbf{E}_{SA}^z) = (1, 0, 0)$, (C9) can be obtained from (C4) and (C6):

$$\frac{\partial \mathbf{E}_x^2}{\partial z^2} - k^2\mathbf{E}_x = 0, \tag{C9}$$

where $k = \sqrt{-i\omega\mu_0(1+\chi_{yy})\sigma_{xx}}$.

Solving (C9) and considering that $\mathbf{E}_x = 0$ when $z \to \infty$, we get

$$\mathbf{E}_x = Ae^{-kz}, \tag{C10}$$

and according to (C4),

$$\mathbf{H}_y = \frac{1}{\sqrt{-i\omega\mu_0(1+\chi_{yy})\rho_{xx}}} Ae^{-kz}. \tag{C11}$$

Therefore, equation (12)–(14) can be obtained for Source A:

$$\mathbf{H}_y^A = \frac{1}{\sqrt{-i\omega\mu_0(1+\chi_{yy})\rho_{xx}}}\mathbf{E}_x^A, \tag{C12}$$

$$\mathbf{H}_x^A = 0, \tag{C13}$$

$$\mathbf{E}_y^A = 0. \tag{C14}$$

Similarly, for Source B: $\mathbf{E}_B = (\mathbf{E}_B^x, \mathbf{E}_B^y, \mathbf{E}_B^z) = (0, 1, 0)$, equation (15)–(18) can be obtained:

$$\mathbf{H}_x^B = \frac{1}{\sqrt{-i\omega\mu_0(1+\chi_{xx})\rho_{yy}}}\mathbf{E}_y^B, \tag{C15}$$

$$\mathbf{H}_y^B = 0, \tag{C16}$$

$$\mathbf{E}_x^B = 0. \tag{C17}$$

Finally, the apparent resistivities in axial conductive and magnetic anisotropic media can be obtained:

$$\rho_a^{xx} = \frac{1}{\omega\mu_0}|Z_{xx}|^2 = \frac{1}{\omega\mu_0}\left|\frac{\mathbf{E}_x^A\mathbf{H}_y^B - \mathbf{E}_x^B\mathbf{H}_y^A}{\mathbf{H}_x^A\mathbf{H}_y^B - \mathbf{H}_x^B\mathbf{H}_y^A}\right| = 0, \tag{C18}$$

$$\rho_a^{xy} = \frac{1}{\omega\mu_0}|Z_{xy}|^2 = \frac{1}{\omega\mu_0}\left|\frac{\mathbf{E}_x^B\mathbf{H}_x^A - \mathbf{E}_x^A\mathbf{H}_x^B}{\mathbf{H}_x^A\mathbf{H}_y^B - \mathbf{H}_x^B\mathbf{H}_y^A}\right|$$
$$= (1+\chi_{yy})\rho_{xx}, \tag{C19}$$

$$\rho_a^{yx} = \frac{1}{\omega\mu_0}|Z_{yx}|^2 = \frac{1}{\omega\mu_0}\left|\frac{\mathbf{E}_y^A\mathbf{H}_y^B - \mathbf{E}_y^B\mathbf{H}_y^A}{\mathbf{H}_x^A\mathbf{H}_y^B - \mathbf{H}_x^B\mathbf{H}_y^A}\right|$$
$$= (1+\chi_{xx})\rho_{yy}, \tag{C20}$$

$$\rho_a^{yy} = \frac{1}{\omega\mu_0}|Z_{yy}|^2 = \frac{1}{\omega\mu_0}\left|\frac{\mathbf{E}_y^B\mathbf{H}_x^A - \mathbf{E}_y^A\mathbf{H}_x^B}{\mathbf{H}_x^A\mathbf{H}_y^B - \mathbf{H}_x^B\mathbf{H}_y^A}\right| = 0. \tag{C21}$$